ACS APPLIED MATERIALS & INTERFACES

www.acsami.org

Research Article

Effect of High-Anisotropic Co^{2+} Substitution for Ni^{2+} on the Structural, Magnetic, and Magnetostrictive Properties of $NiFe_2O_4$: Implications for Sensor Applications

Mudalagiriyappa Satish, Hadonahalli Munegowda Shashanka, Sujoy Saha, Keerthi Haritha, Debabrata Das, Pendaranahalli Nadikeraiah Anantharamaiah,* and C. V. Ramana*

Cite This: *ACS Appl. Mater. Interfaces* 2023, 15, 15691−15706

Read Online

ACCESS | Metrics & More | Article Recommendations | Supporting Information

ABSTRACT: This work reports on the effect of substituting a low-anisotropic and low-magnetic cation (Ni^{2+}, $2\mu_B$) by a high-anisotropic and high-magnetic cation (Co^{2+}, $3\mu_B$) on the crystal structure, phase, microstructure, magnetic properties, and magnetostrictive properties of $NiFe_2O_4$ (NFO). Co-substituted NFO ($Ni_{1-x}Co_xFe_2O_4$, NCFO, $0 \leq x \leq 1$) nanomaterials were synthesized using glycine-nitrate autocombustion followed by postsynthesis annealing at 1200 °C. The X-ray diffraction measurements coupled with Rietveld refinement analyses indicate the significant effect of Co-substitution for Ni, where the lattice constant (a) exhibits a functional dependence on composition (x). The a-value increases from 8.3268 to 8.3751 Å (±0.0002 Å) with increasing the "x" value from 0 to 1 in NCFO. The a−x functional dependence is derived from the ionic-size difference between Co^{2+} and Ni^{2+}, which also induces grain agglomeration, as evidenced in electron microscopy imaging. The chemical bonding of NCFO, as probed by Raman spectroscopy, reveals that Co(x)-substitution induced a red shift of the $T_{2g}(2)$ and $A_{1g}(1)$ modes, and it is attributed to the changes in the metal−oxygen bond length in the octahedral and tetrahedral sites in NCFO. X-ray photoelectron spectroscopy confirms the presence of Co^{2+}, Ni^{2+}, and Fe^{3+} chemical states in addition to the cation distribution upon Co-substitution in NFO. Chemical homogeneity and uniform distribution of Co, Ni, Fe, and O are confirmed by EDS. The magnetic parameters, saturation magnetization (M_S), remnant magnetization (M_r), coercivity (H_C), and anisotropy constant (K_1) increased with increasing Co-content "x" in NCFO. The magnetostriction (λ) also follows a similar behavior and almost linearly varies from −33 ppm ($x = 0$) to −227 ppm ($x = 1$), which is primarily due to the high magnetocrystalline anisotropy contribution from Co^{2+} ions at the octahedral sites. The magnetic and magnetostriction measurements and analyses indicate the potential of NCFO for torque sensor applications. Efforts to optimize materials for sensor applications indicate that, among all of the NCFO materials, Co-substitution with $x = 0.5$ demonstrates high strain sensitivity (-2.3×10^{-9} m/A), which is nearly 2.5 times higher than that obtained for their intrinsic counterparts, namely, $NiFe_2O_4$ ($x = 0$) and $CoFe_2O_4$ ($x = 1$).

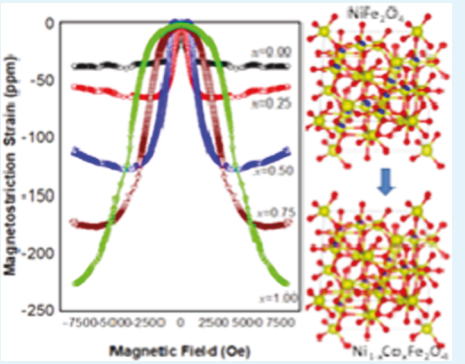

KEYWORDS: *$NiFe_2O_4$, Co-substitution, structure, magnetostriction, strain sensitivity, sensors*

INTRODUCTION

Magnetostriction, in which the physical dimensions of magnetic materials change when a magnetic field is applied, is of great relevance for the development of cutting-edge sensors for automotive and energy technology.[1−4] Magnetostriction often involves a reversible energy exchange between the mechanical form and the magnetic form. In reality, magnetostrictive materials can be used in numerous industrial applications, particularly in sensors and actuators, because of their capacity to convert a precise amount of energy from one form to another.[5−9] As a result, currently, there is an enormous interest in one particular group or family of functional materials that exhibit magnetostriction and are called magnetostrictive smart materials (MSMs).[2,3,6,8−10] Due to their magnetoelastic properties, these MSMs are also widely used in a variety of technological applications, such as stress sensors, actuators, magnetostrictive filters, controlled fuel injection systems, sensors, sonar transducer systems, etc. Alloy-based MSMs, such as Terfenol-D[11] and Galfenol,[12] exhibit exceptional magnetostriction strain (λ) but only in the single-crystal form. However, these materials possess lower magnetostriction values (λ and $d\lambda/dH$) in the polycrystalline or nanocrystalline form. Therefore, the design and development of metal oxide-

Received: December 23, 2022
Accepted: February 22, 2023
Published: March 20, 2023

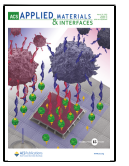

https://doi.org/10.1021/acsami.2c23025
ACS Appl. Mater. Interfaces 2023, 15, 15691−15706

based MSMs as alternatives to alloy-based MSMs have, on the other hand, been the subject of active research in recent years. Specifically, ferrite-based materials are attractive due to their low cost of synthesis and processing, chemical and mechanical stability, low eddy current, appropriateness for high-frequency devices, etc.[13−19] It has been claimed that some perovskite-type manganates are extremely magnetostrictive materials, but as the material temperature rises to RT, their magnetostriction gradually dissipates.[20,21] However, it is essential to have/develop metal oxide-based MSMs with high magnetostriction strain (λ) and strain sensitivity ($d\lambda/dH$) for room-temperature applications. In this context, cobalt ferrite ($CoFe_2O_4$; CFO) and nickel ferrite ($NiFe_2O_4$; NFO) with demonstrated and greater magnetostriction at room temperature are of considerable interest.[18,22−25]

Structurally, both CFO and NFO are characterized as cubic-spinel-structured ferrites.[15,26−28] However, while NFO is a soft magnetic phase, CFO is a hard magnetic phase. Similar to their magnetic features, NFO is a soft magnetostrictive phase, whereas CFO is a hard magnetostrictive phase. CFO exhibits high magnetostriction ($\lambda_{||} \sim -100$ to -400 ppm) only at higher applied magnetic fields because of its hard magnetic and high anisotropy characteristics. Among spinel-type ferrite systems, hard magnetic and magnetostrictive characteristics of CFO are attributed to a strong spin−orbit coupling of Co^{2+} ions residing at the B-sites. CFO in thin-film polycrystalline forms also demonstrates superior magnetic properties at both RT and low temperatures.[29−31] Shirsath et al. studied the magnetic properties of CFO thin films grown on different substrates and reported superior magnetocrystalline anisotropy, saturation magnetization, and coercivity for the fabricated CFO films.[29−31] In contrast, NFO exhibits a soft magnetic property and low anisotropy, with a magnetostriction observed in the range of -25 to -40 ppm at comparatively low magnetic fields. One may be able to adjust the magnetostrictive characteristics of NFO by substituting suitable metal ions. The main determinants of the degree of magnetostriction of a ferrite are the kind of substituents (magnetic/nonmagnetic), the quantity (low/high), and the crystallographic site preferences (tetrahedral/octahedral). There are some efforts in the literature where metal-ion dopants were employed to obtain the tunable magnetic and magnetostrictive characteristics of NFO materials using various methods.[25,32−35]

Atif et al.[32] studied the effect of nonmagnetic metal-ion (Zn^{2+}) substitution for Ni^{2+} in $NiFe_2O_4$ on the magnetostrictive properties and reported a decrease in λ_{max} with an increase in the Zn content, and it was attributed to a reduction in magnetocrystalline anisotropy. Bharathi et al.[18,24] showed marginal changes in the magnitude of magnetostriction of sintered nickel ferrite samples after replacing a small fraction of Fe^{3+} by large-sized rare-earth ions such as Dy^{3+}, Gd^{3+}, Ho^{3+}, and Sm^{3+}, and all of these samples were prepared through the solid-state reaction method.[18,24] Mathe et al.[25] synthesized Ni-substituted cobalt ferrite samples ($Ni_xCo_{1-x}Fe_2O_4$) using a coprecipitation method and low-temperature (600 °C) synthesis, and their magnetostriction measurements were carried out along the parallel direction ($\lambda_{||}$). A systematic decrease in the magnetostriction from -65 ppm for $CoFe_2O_4$ to -5 ppm for $NiFe_2O_4$ was reported. Bhame et al.[33] also studied the effect of replacing Co^{2+} by Ni^{2+} in cobalt ferrite ($Ni_xCo_{1-x}Fe_2O_4$) samples made through the solid-state reaction method on the magnetostrictive properties and indicated that the composition with $x = 0.2$ is suitable for application due to its strain sensitivity (-56×10^{-6} m/A) and magnetostriction (-164 ppm). It was shown that nonmagnetic cations (Mg^{2+} and In^{3+}) with different crystallographic site preferences, as substituted for Fe^{3+} in $NiFe_2O_4$, have a considerable impact on the magnetostriction magnitude in sintered nickel ferrite.[34] Recently, Mane et al.[35] reported the magnetostriction characteristics for microwave-annealed Ni-substituted CFO ($Co_{1-x}Ni_xFe_2O_4$) nanoparticles of size ∼20 nm. Out of all of the compositions studied, $CoFe_2O_4$ and $Co_{0.9}Ni_{0.1}Fe_2O_4$ samples showed the highest magnetostriction parameters (maximum magnetostrictive coefficient of -180 ppm and strain sensitivity of -0.0117 ppm/Oe (-1.47×10^{-9} m/A)).[35] The low magnetostriction parameters associated with these reported materials are most probably due to the nanostructure nature of the materials. This is because, at the nanoscale dimensions of these materials, the defects play a vital role in mitigating the magnetostriction. Magnetic properties of nanocrystalline Ni-Co-ferrites doped with rare-earth elements were also studied and have been reported in the literature.[36,37] Note that it is always better to develop dense ceramic ferrite products with enhanced magnetostrictive properties for desirable applications. Herein, we considered Co^{2+} to replace Ni^{2+} in $NiFe_2O_4$ since it has a larger magnetic moment and a higher anisotropy than Ni^{2+}, which means that this substitution can also result in increased magnetostriction and magnetization. Using this approach, which eliminates the need for complex cation doping and/or expensive rare-earth ions, it may be possible to find an ideal chemical composition for an intermediate phase that lies between the hard (CFO) and soft (NFO) magnetostrictive phases and can exhibit more superior magnetostrictive properties than the end-members of the series ($Ni_{1-x}Co_xFe_2O_4$). Therefore, $Ni_{1-x}Co_xFe_2O_4$ ceramic materials in the nanocrystalline form were made using an autocombustion chemical method and sintered at a higher temperature (1200 °C/2 h) to obtain dense products. Even though numerous wet-chemical methods, such as coprecipitation, sol−gel, hydrothermal, microwave−assisted, thermal decompositions, etc., are available for ferrite synthesis,[38,39] the autocombustion method (glycine-nitrate solution combustion) has been adopted in the present work because of three major reasons/advantages. First of all, the autocombustion method is simple and it is a direct or single-step synthesis process, which eliminates the need for postsynthesis heat treatment for phase development. The second reason is the yield in autocombustion synthesis. In this method, a large quantity of samples (which is a major requirement for magnetostriction measurements through strain gauge) can be obtained in a short span of time, that too in the single phase. The third and final specific feature that is attractive for ferrite synthesis is the flexibility and control over particle size. Depending on the glycine (which acts as a fuel for combustion) and nitrate (acts as an oxidizer for combustion) ratio, we can tune the final ferrite particle size. Here, in view of all of the above-mentioned advantages, we employed autocombustion for $Ni_{1-x}Co_xFe_2O_4$ materials' synthesis, but we have fixed the glycine content (1 mole per mole of metal ion) so that complete combustion takes place without any leftover of the contents. The magnetostriction strain curves were measured for sintered $Ni_{1-x}Co_xFe_2O_4$ compositions and compared. In comparison to the other compositions in the series, the material with $x = 0.5$ displayed superior magnetostriction strain ($\lambda_{max} = -160$ ppm) and strain sensitivity ($(d\lambda/dH)_{max} = -2.3 \times 10^{-9}$ m/A) at lower magnetic fields.

https://doi.org/10.1021/acsami.2c23025
ACS Appl. Mater. Interfaces 2023, 15, 15691−15706

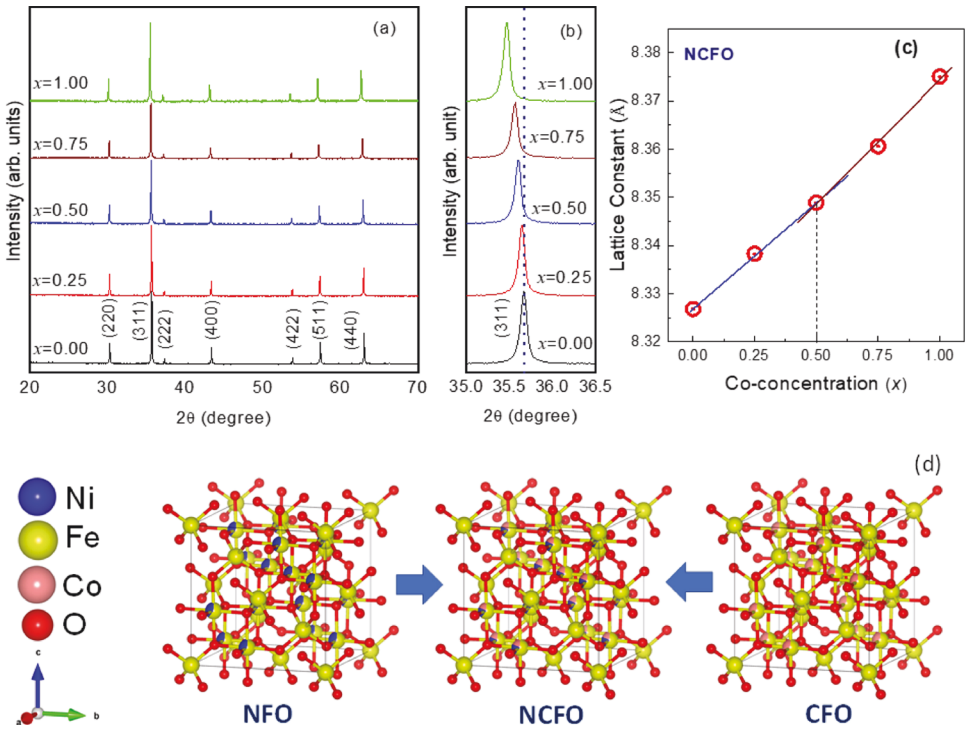

Figure 1. XRD data of NCFO samples. (a) XRD data of NCFO samples with variable Co-concentrations. The peaks due to diffraction from various crystal planes are as indexed. Spinel ferrite formation is evident in the XRD patterns. (b) Enlarged view of the (311) peak of NCFO samples. The data indicate a systematic peak shift with increasing Co-concentration in NCFO. (c) Variation of the lattice constant as a function of the Co-content in NCFO. Two distinct linear slopes with a deviation at composition $x = 0.5$ is evident. (d) Cubic-spinel crystal structure of pure $NiFe_2O_4$, Co-substituted (mixed-cation) NCFO, and pure $CoFe_2O_4$.

MATERIALS AND METHODS

Synthesis. The autocombustion method, reported elsewhere,[40] has been adapted to synthesize the $Ni_{1-x}Co_xFe_2O_4$ ($0 \leq x \leq 1$) samples using metal nitrates ($Ni(NO_3)_2{\cdot}6H_2O$, 99%, Loba Chemie; $Co(NO_3)_2{\cdot}6H_2O$, 99%, SD fine Chem; $Fe(NO_3)_3{\cdot}9H_2O$, 98%, SD fine Chem; and glycine (NH_2CH_2COOH), 99.5%, Merck) as starting materials. Briefly, a homogeneous mixture of metal nitrates, taken according to nominal composition, solution, and glycine (1 mol/M^+) was heated on a hot plate (~200 °C). Since the adequate amount of glycine was taken, the reactions of all of the compositions underwent complete combustion, yielding corresponding stable metal oxide (magnetic phase) powders in a porous nature. As-obtained ferrite powders were thoroughly ground to fine particles using an agate mortar and pestle. It is confirmed from lab magnets that all synthesized compositions are magnetic in nature, meaning that the heat released during autocombustion was adequate enough to develop a spinel phase with a magnetic nature and no requirement for postsynthesis calcination. Using 2% PVA solution as a powder binding agent, the ferrite powders were molded as disc-shaped (12 mm dia × 4 mm thickness) pellets by applying 5 N uniaxial pressure. The compacted green pellets were heated from room temperature (RT) to 1200 °C at a heating rate of 5 °C/min (using a programmable furnace), and then, they were held at 1200 °C for 2 h. Afterward, they were cooled to RT, naturally. Note that all compositions were processed and sintered under the same conditions, for better comparison.

Characterization. To carry out the structural analysis and evaluate the phase purity on the sintered products, the pellets of $Ni_{1-x}Co_xFe_2O_4$ samples were ground into fine powders, and room-temperature powder XRD data were recorded, in the 2θ range from 10 to 80° with a step size of 0.01°, by means of a high-resolution powder diffractometer (SmartLab, Rigaku) equipped with a Cu rotating anode operating in the Bragg-Brentano geometry and fitted with a Johansson monochromator to eliminate Cu $K\alpha_2$ radiation. The samples of NCFO were also examined using high-resolution transmission electron microscopy (TEM) measurements. The TEM measurements were made using an FEI Tecnai G2 F30 with an applied voltage of 300 kV. Crystal structure, morphology, and microstructure of the ferrite samples were studied to understand the effect of Co-cation substitution in NFO. As-synthesized NCFO samples were employed for all of the TEM measurements. A Quanta 200, FEI scanning electron microscopy (SEM) instrument was employed to capture SEM images from the interior regions of the sintered pellets. For each sample, multiple images in different scales and magnifications were captured from different regions of the sintered pellets so as to assess the homogeneity in grain size distributions and shape. SEM images of the NCFO samples were acquired in the same scale bar (2 μm) and magnification for a reasonably good assessment.

Elemental mapping tests were carried out utilizing a scanning electron microscope (TESCAN VEGA3 LMU) instrument to look into the chemical/elemental distribution of different ions on the surface of the samples and to calculate their atomic percentage (atom %). The equipment has an EDS detector to measure the weight and atomic percentages (wt % and atom %) of different elements in the samples. For all of the elements in NCFO (Co, Ni, Fe, and O), mappings were acquired and quantification of each and every element was made. Finally, the composition was also validated with the targeted composition of the synthesis process. Raman spectroscopic measurements were made to see the Co-substitution-induced changes in Ni-ferrite materials. Using an IndiRam Raman spectrophotometer, the Raman spectra were recorded on the smooth surface of the sintered pellets by exciting the samples using a 532 nm laser radiation. XPS data of NCFO samples were recorded using a Thermo Kalpha+ spectrometer. An Al Kα X-ray source (energy ≈ 1486.6 eV) was used for the generation of photoelectrons from the NCFO sample surface. To characterize and derive quantitative information on the effect of Co-substitution, we analyzed the detailed core-level spectra of respective cations in NCFO. We employed previously documented

https://doi.org/10.1021/acsami.2c23025
ACS Appl. Mater. Interfaces 2023, 15, 15691−15706

procedures and techniques that were very successful in analyzing the surface chemistry of simple and complex oxides.

Magnetization hysteresis loops of the samples were measured at room temperature using a vibrating sample magnetometer (VSM, lakeshore) in the field range -20 kOe $\leq H \leq 20$ kOe with a step size of 50 Oe. To determine the Curie temperature (T_C) of the samples, thermomagnetization curves were recorded above room temperature in the presence of a constant magnetic field (100 Oe). For magnetostriction measurements, 350 Ω strain gauge was cemented over the smooth surface of the sintered pellet using a suitable adhesive and dried at 85 °C. The room-temperature magnetostriction strain curves of the samples were measured along the direction parallel to the applied H (-8 kOe $\leq H \leq +8$ kOe). The experimental setup used and the schematic diagram of magnetostriction measurements for the sintered $Ni_{1-x}Co_xFe_2O_4$ samples using the strain gauge method are illustrated in Figure S1 (Supporting Information).

RESULTS AND DISCUSSION

Structure and Phase: XRD and Rietveld Refinement. XRD data of NCFO samples are shown in Figure 1. The XRD patterns (Figure 1a) show a good signal-to-noise ratio due to the high crystallinity reached by the sintering. As indexed for the NFO sample, crystal planes (220), (311), (222), (400), (422), (511), and (440) are the ones that are responsible for the Bragg diffraction peaks at 2θ values of 30.27, 35.67, 37.33, 43.37, 53.82, 57.39, and 63.04°, respectively. The formation of a single phase material with a cubic-spinel-type structure and an Fd3̄m space group (JCPDS card no. 10-0325)[41] is indicated by the presence of these peaks in the XRD data. The Co-substituted NCFO samples exhibit the same type patterns as pristine NFO, and they are without secondary phase peaks. This observation indicates that the substituted Co^{2+} ions are successfully incorporated into the lattice of Ni-ferrite, resulting in a perfect solid solution with single phase material formation. The enlarged region of the (311) peak is shown in Figure 1b, where the progressive peak shift toward lower 2θ values with increasing x is evident. After replacing Ni^{2+} in NFO with Co^{2+}, changes in the lattice constant (crystal structure parameter) and peak shift can be anticipated due to the larger ionic size of Co^{2+}.

To obtain the structural parameters of NCFO samples, Rietveld refinement was carried out on the XRD patterns using a Fullprof program. The results of refinements are shown in Figure 2, while the lattice constant and fitting parameters are listed in Table 1. In Figure 2, the calculated pattern is represented by the solid red curve and the closed black circles are the experimental data. The blue curve depicts the disparity between the calculated and observed patterns. The foundation of the XRD profile was fitted by direct insertion, while pseudo-Voigt capability was utilized to fit the pinnacle profile. Scale factor, zero correction, background, half width, lattice constant, atom coordinates, and the isotropic thermal parameter (B_{iso}) of cations were varied throughout the refinement. The insets of Figure 2 make this clear, while the χ^2 (goodness-of-fit) values given in Table 1 indicate that all of the compositions analyzed in this work were found to be well-matched by means of good fits. The lattice constant, 8.3268 Å, for $x = 0$, i.e., intrinsic NFO, is in good agreement with those reported for Ni-ferrite in the literature.[34] Variation of lattice constant as a function cobalt content x is shown in Figure 1c.

Two distinct linear slopes with a change at $x = 0.5$ can be seen in Figure 1c. Initially, the lattice constant increases linearly from 8.3268 for $x = 0$ to 8.3489 Å for $x = 0.5$, and it deviates from linearity at $x > 0.5$. Beyond $x = 0.5$, again the

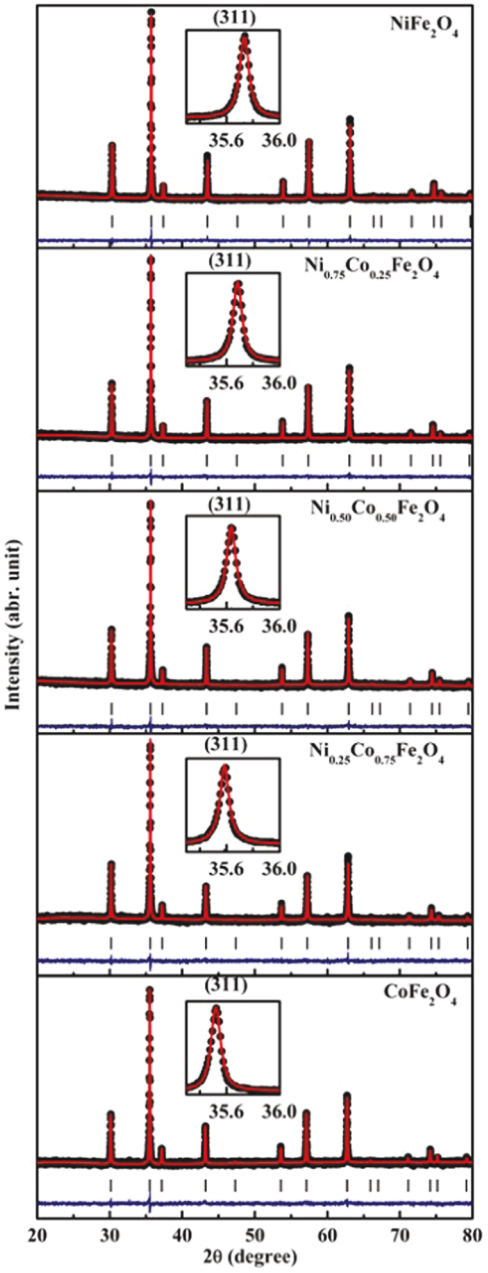

Figure 2. Rietveld refined XRD patterns of the NCFO samples.

Table 1. Refined Lattice Constant, Atomic Parameters, and Isotropic Thermal Parameters of $Ni_{1-x}Co_xFe_2O_4$ (x = 0, 0.25, 0.5, 0.75, and 1)[a]

	$x = 0$	$x = 0.25$	$x = 0.5$	$x = 0.25$	$x = 1.0$
a (Å) (±0.0002)	8.3268	8.3383	8.3489	8.3610	8.3751
B_{iso} (A site)	0.303	0.756	0.614	0.489	0.754
B_{iso} (B-site)	0.407	0.949	0.815	0.653	0.243
O (x, x, x)	0.25788	0.25500	0.25565	0.25342	0.25403
R_p	2.30	2.10	1.91	1.78	1.43
R_{wp}	2.69	2.67	2.31	2.25	1.88
R_{exp}	2.44	2.19	2.06	2.00	1.51
χ^2	1.22	1.49	1.39	1.27	1.54

[a]The respective Wyckoff sites for these AB_2O_4 spinel ferrites are A 8b (1/8, 1/8, 1/8); B 16c (0.5, 0.5, 0.5) and O32e (x, x, x) within the cubic space group $Fd\bar{3}m$.

https://doi.org/10.1021/acsami.2c23025
ACS Appl. Mater. Interfaces 2023, 15, 15691−15706

changes are linear from 8.3489 for $x = 0.5$ to 8.3751 Å for $x = 1$ ($CoFe_2O_4$). The lattice constant increase with cobalt content x is principally due to the substitution of smaller cation Ni^{2+} (ionic sizes are 0.55 Å at 4-fold and 0.69 Å at 6-fold coordination) by larger cation Co^{2+} (ionic sizes are 0.58 Å at 4-fold and 0.745 Å at 6-fold coordination) in $NiFe_2O_4$. A slight deviation of lattice constant from linearity at $x = 0.5$ is presumably due to changes in the cation distribution, as nickel ferrite is virtually inverse spinel (Figure 1d), whereas cobalt ferrite is of a mixed spinel stricture (Figure 1d; middle panel). At the start, up to $x = 0.5$, Co^{2+} ions are being substituted for Ni^{2+} predominantly at the octahedral site (B-site) and for $x > 0.5$, along with octahedral site occupancy, some fractions of Co^{2+} start occupying the tetrahedral site (A-site) and shift an equivalent amount of Fe^{3+} from the A-site to the B-site, making the system transform from a nearly inverse spinel structure to a more and more mixed spinel structure (see Figure 1d for a schematic representation of this structural sequence).

Surface Morphology and Microstructure: TEM and SEM. To further investigate the crystal quality, local microstructure, and grain morphology, NCFO samples were analyzed with TEM, and the data are presented in Figure 3.

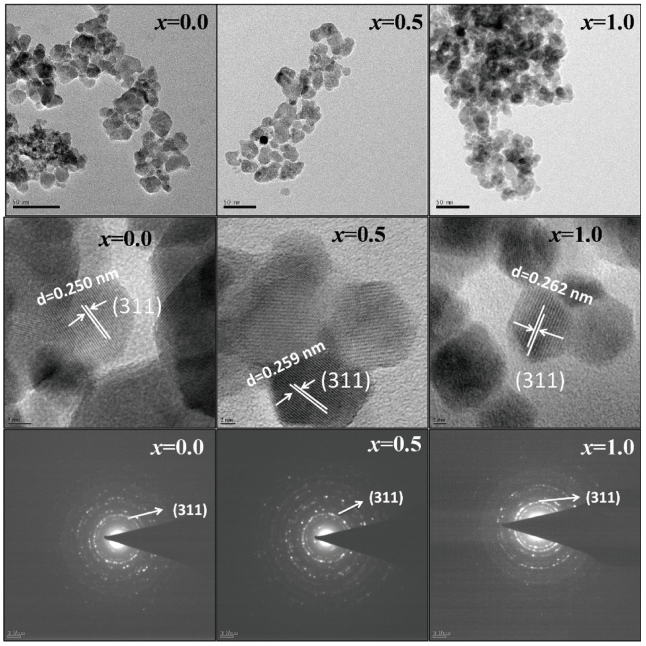

Figure 3. (a) TEM images (top row), (b) high-resolution images (middle row), and (c) selected area electron diffraction (SAED) patterns (bottom row) of as-synthesized NCFO samples with $x = 0.0$, 0.5, and 1.0.

It is clear from the TEM dark-field images (shown in the top row) that all of the ferrite particles are approximately spherical in shape. Both smaller and larger ferrite particles can be seen in these images. The high-resolution TEM images, shown in the middle row, revealed the presence of lattice fringes that signifies the crystalline nature of the ferrite particles synthesized. Based on the d-spacing (interplanar spacing) measured from the images using a digital micrograph, the exposed crystalline plane is labeled as (311). Interestingly, the d-spacing of the (311) plane increases from 0.250 nm for $x = 0.0$ to 0.262 nm for $x = 1.0$ due to substitution of the larger cation Co^{2+} for the smaller cation Ni^{2+} in NFO. These results are corroborated with XRD and Rietveld refinement data as discussed in the previous section. The presence of concentric circles, due to different crystal planes, in selected area electron diffraction patterns of the samples, shown in the bottom row, indicates the nanocrystalline nature of the samples. Overlapping of nanocrystals produces the ring patterns seen in the SAED patterns.

Surface morphological features of NCFO samples investigated by capturing SEM images from the interior regions of the cracked pellets are shown in Figure 4. The SEM images reveal that Co-substitution for Ni in NFO influences the morphology evolution in terms of grain size and shape. Intrinsic NFO ($x = 0$) exhibits smaller grains with a nearly uniform size distribution. However, as the Co-content (x) increases, the grain size steadily increases in NCFO. Furthermore, grain size distribution in Co-substituted samples is quite heterogeneous, with only a few of the grains being irregular in shape. Corroborating with XRD studies, and particularly with lattice constant enhancement, the grain size increase with x can be attributed to the larger ionic size of Co^{2+} compared to Ni^{2+}. The larger ions promote grain growth appreciably by sinking the energy barrier between the grains. Cobalt substitution-induced grain growth and size increase have been observed in nanocrystalline Ni-ferrite.[42] To quantify the microstructure changes as a function of Co-substitution, grain size distribution histograms for the NCFO samples were made by measuring the individual grains from the SEM images, and the histograms are shown on the individual sample SEM image. It is clear that all of the samples are made of smaller and larger grains, but the average grain size, found in the center of the Gaussian peak, increases from 288 nm for $x = 0.0$ to 625 nm for $x = 1.0$. The size distribution histograms clearly indicate that Co-substitution promotes the nanocrystallites joining together, leading to larger grains, which further grew and almost tripled in size for a Co-content increase from $x = 0$ to 1. Thus, the structure evaluation evaluated by XRD and refinement analyses and SEM morphology imaging analysis indicates that the Co-substitution significantly affects the crystal structure and morphology, while the cubic-spinel phase is maintained in all of the NCFO samples.

Chemical Homogeneity and Chemical Bonding: EDS and Raman Spectroscopy. The EDS data of sintered NCFO samples are shown in Figure 5. All of the elements of the respective NCFO materials are found in the EDS spectra, suggesting chemical purity of the samples. Note that the specific energy of X-rays, which are produced when an electron beam bombards the sample, provides the signature of the atom from which it is emitted. Therefore, the elemental mapping data validates our synthesis strategy, which successfully enabled Co-substitution into NFO, as well as the chemical homogeneity of the NCFO samples. In each EDS spectrum, the weight and atomic % of the sample elements are listed in the form of a table shown in the inset. Note here that these spectra as well as weight and atomic percentages are taken from one specific spot of the samples, and these percentages would be different for different spots of the sample. The obtained atomic percentage of the samples, taken at a specific spot, is comparable to the target atomic percentage of the compositions.

To investigate the distribution of various ions in the NCFO samples, elemental mapping of the materials was carried out on the selected sample region. The results obtained are shown in Figure 6. All elements of the samples are more or less distributed homogeneously, without segregation.

https://doi.org/10.1021/acsami.2c23025
ACS Appl. Mater. Interfaces 2023, 15, 15691−15706

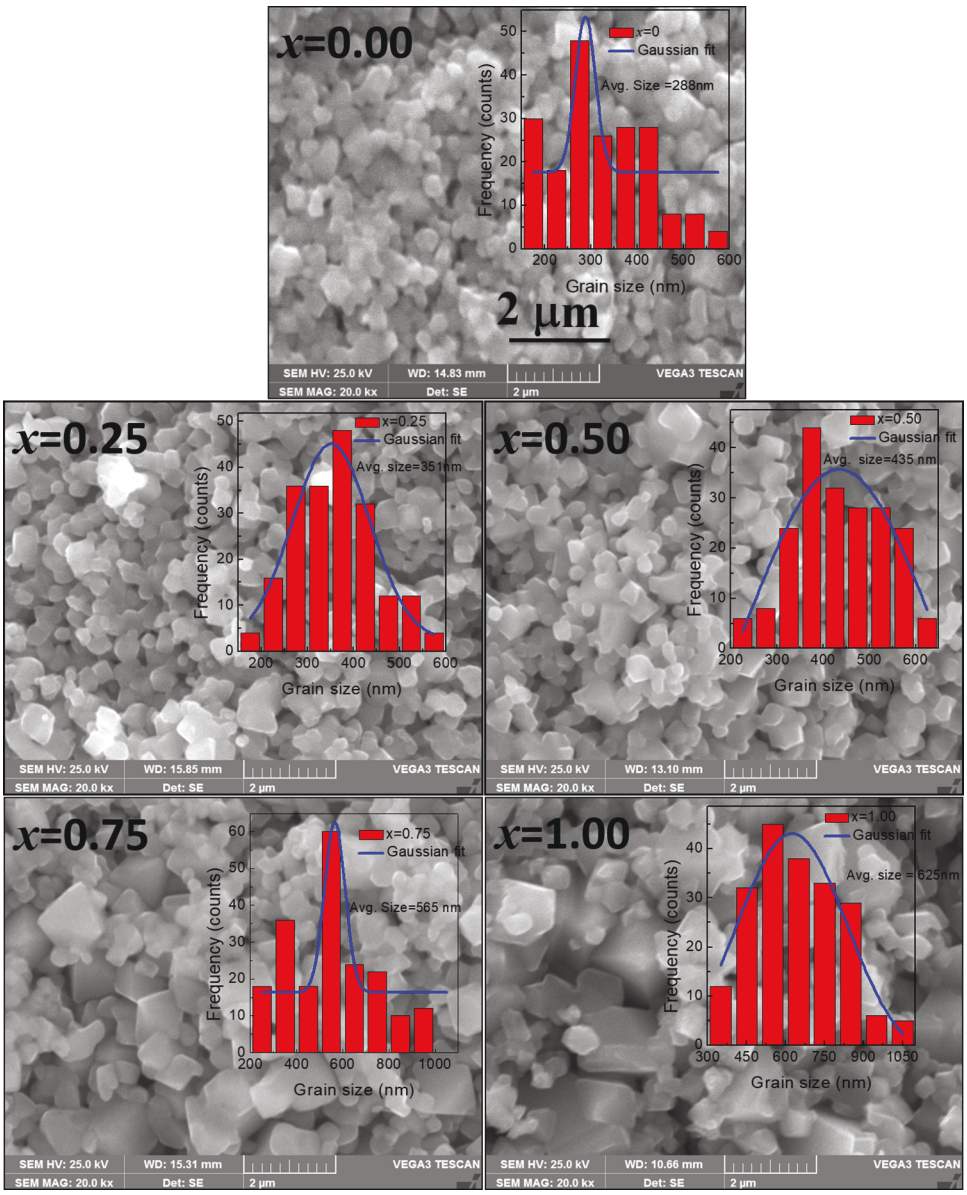

Figure 4. SEM images of NCFO samples. The effect of increasing Co-content on the morphology evolution of NCFO samples is evident in the SEM images.

Having understood the chemical quality and homogeneity of NCFO samples, we now turn our attention to the chemical bonding in NCFO as a function of *x*. Raman spectroscopy can be employed as a nondestructive and complementary tool[43,44] to gauge numerous spinel ferrite systems, as Raman bands are meticulously sensitive to any change in local structural parameters such as bond lengths, bond angles, and cation distributions of the spinel ferrite systems.[15,45,46] Since XRD analysis revealed that the lattice constant of NCFO increases linearly with increasing Co-content, Raman spectroscopy analyses were primarily utilized to determine how the Co-substitution affects the chemical bonding and the specific Raman bands of the tetrahedral and octahedral sites of the spinel-structured Ni-ferrite.[47] The Raman spectra of NCFO samples, as shown in Figure 7, exhibit five major characteristic bands, namely, A_{1g}, E_g, and $3T_{2g}$, as predicted based on the factor group analysis.[15,45,46] In the case of NFO ($x = 0$), each Raman band has a shoulder stretched out at lower wavenumbers due to the inverse spinel nature of the sample. The main $A_{1g}(1)$ band located at 691 cm^{-1} has been assigned to the symmetric vibration of Fe−O bonds in the FeO_4 (tetrahedral) unit, and its shoulder at a lower wavenumber (~660 cm^{-1}), designated as $A_{1g}(2)$, arises from the vibration of Ni−O bonds in the NiO_4 (tetrahedral) unit.[34,47] Similarly, the triply degenerate $T_{2g}(2)$ band at ~478 cm^{-1} is due to the symmetric vibration of Fe−O bonds in the FeO_6 (octahedral) unit and its shoulder at a lower wavenumber is due to the vibration of Ni−O bonds in the NiO_6 unit.[34,47]

The Raman mode shift as a function of Co-substitution is the most important observation made in the data shown in Figure 7a−c. It is evident that, upon Co-substitution, both $A_{1g}(1)$ (tetrahedral) and $T_{2g}(2)$ (octahedral) bands shift steadily toward lower wavenumbers (red shift). The substantial or noticeable red shift is primarily attributed to changes (increase) in the bond lengths of tetrahedral and octahedral units. As the Co−O bond length is longer than the Ni−O bond length in both tetrahedral and octahedral environments, CoO_4 and CoO_6 units vibrate at lower frequencies compared

https://doi.org/10.1021/acsami.2c23025
ACS Appl. Mater. Interfaces 2023, 15, 15691−15706

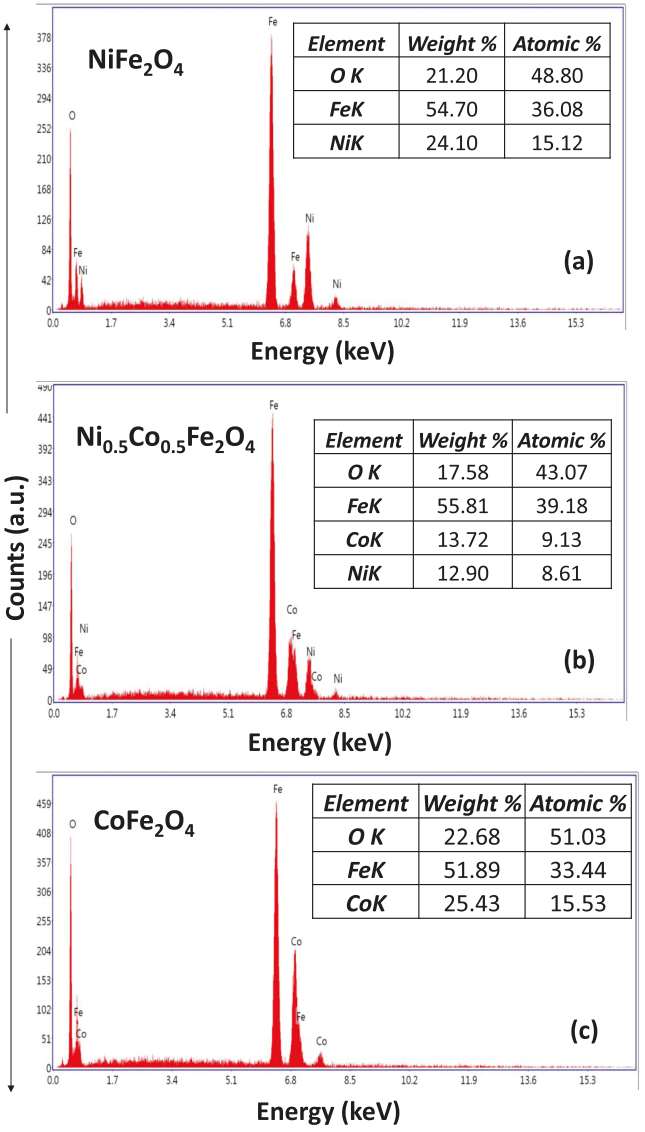

Figure 5. EDS data of NCFO samples. The wt % and atom % determined are shown in the inset as tables for every spectrum collected.

to the vibrational frequencies of NiO_4 and NiO_6 units. As a result, the Raman modes experience a red shift in all of the Co-substituted NFO samples compared to intrinsic NFO. To further understand the changes in the chemical bonding and corroborate with structural changes probed in XRD, variations in the peak positions of $A_{1g}(1)$ and $T_{2g}(2)$ bands as a function of Co-content in NCFO are shown in Figure 7b,c, respectively. It is evident (Figure 7b,c) that the peak positions of both $A_{1g}(1)$ and $T_{2g}(2)$ bands decrease linearly and rapidly toward lower wavenumbers up to the composition $x = 0.5$. For $x \geq 0.5$, the positions of the bands continue to decrease linearly but at a slower pace. Thus, based on the Raman spectral analysis, we believe that the composition with $x = 0.5$ is a crossover region for cation distribution in NCFO. Up to $x = 0.5$, Ni^{2+} ions are being replaced by Co^{2+} at the octahedral sites. However, for $x > 0.5$, in addition to occupation at octahedral sites, some fraction of Co^{2+} may start occupying tetrahedral sites and push the same amount of Fe^{3+} from the tetrahedral sites to the octahedral sites, making the system a fully mixed spinel structure. Thus, Raman analyses support the interpretation of XRD results.

Chemical Valence States and Cation Distribution: XPS. Figure S2 shows the XPS survey spectra of NCFO samples. By analyzing the XPS data, element chemical states and cation distribution for particular compositions of NCFO samples were investigated thoroughly. It should be noted that while carbon (C 1s) is utilized as an internal reference, the peak of C 1s with a binding energy (BE) of ~284 eV is visible in all of the NCFO samples. The survey spectra (Figure S2) also show the XPS signals caused by the various elements in the samples, and they are labeled with the appropriate elements (Fe, Co, Ni, and O). In addition, a few extra peaks can also be found in the survey spectra of all three samples, along with the XPS peaks of the constituent elements, and they probably originated from Auger signals (KLL, LMM, etc.).[17,48]

The high-resolution XPS spectra of Ni 2p, Fe 2p, and Co 2p of the NCFO samples with variable Co-contents are presented in Figure 8a–c, respectively. The energy corrections for these spectra were made based on the binding energy of the C 1s peak (fixed at 284.6 eV) and then compared.[49] The shape of the peaks depends prominently on the chemical states of the elements present in the samples.[31] All three elements show two primary peaks with the designations $2p_{3/2}$ and $2p_{1/2}$, as well as satellite (shake-up) peaks at higher binding energies. From the degeneracy $(2J + 1)$, it was discovered that the intensity ratio between $2p_{3/2}$ and $2p_{1/2}$ is almost 2:1.[50−52] For Ni (Figure 8a) and Co (Figure 8b), the intensity of the satellite peaks is comparatively high, whereas it is modest in the case of Fe (Figure 8c), showing that Ni and Co are in the 2+ oxidation state, while Fe is in the 3+ oxidation state. The Ni and Fe XPS peaks of NCFO change steadily toward higher binding energies as the Co-content (x) increases. Another noteworthy finding is that the Ni $2p_{3/2}$ peak is narrower compared to the broader $2p_{3/2}$ peaks of Fe and Co. This is predominantly due to the majority of Ni^{2+} ions occupying a particular crystallographic site (B-site), whereas Fe^{3+} and Co^{2+} are distributed among A- and B-sites of the spinel ferrite lattice.[34,49]

Figures S3–S5, respectively, show the results of the deconvoluted spectra of Ni 2p, Fe 2p, and Co 2p, which were used to gain comprehensive insights into the binding energies of $2p_{3/2}$ and $2p_{1/2}$ components and their satellite peaks as well as the cation distributions. Prior to deconvolution, all elemental spectra were normalized based on the intensity of the $2p_{3/2}$ peak. Tables 2, 3, and 4 list the BE values of Ni^{2+}, Fe^{3+}, and Co^{2+}, respectively. These binding energies are comparable to the values reported for the Ni^{2+}, Fe^{3+}, and Co^{2+} ions in the literature.[17,49−53]

The cation distribution in tetrahedral (A-site) and octahedral (B-site) sites for $x = 0.0$, 0.5, and 1.0 samples has been estimated through area under the XPS peaks of A-site and B-site, and the obtained results are tabulated in Table 5. The $NiFe_2O_4$ and $CoFe_2O_4$ samples are clearly mixed spinel structures and nearly inverse structures, respectively, as shown by the cation distributions, and these distributions are nearly comparable to the reported cation distributions for Co- and Ni-ferrite samples extracted via Mossbauer analysis. The effect of Co-content into NFO is to drive the mechanism and replace more and more Ni^{2+} at the octahedral sites by the high-anisotropic Co^{2+}, as x increases in NCFO.

The deconvoluted XPS spectra of the O 1s core level for the samples with $x = 0–1$ are shown in Figure 9. The shape of the O 1s peak for the sample $x = 0$ is noticeably different from that

https://doi.org/10.1021/acsami.2c23025
ACS Appl. Mater. Interfaces 2023, 15, 15691−15706

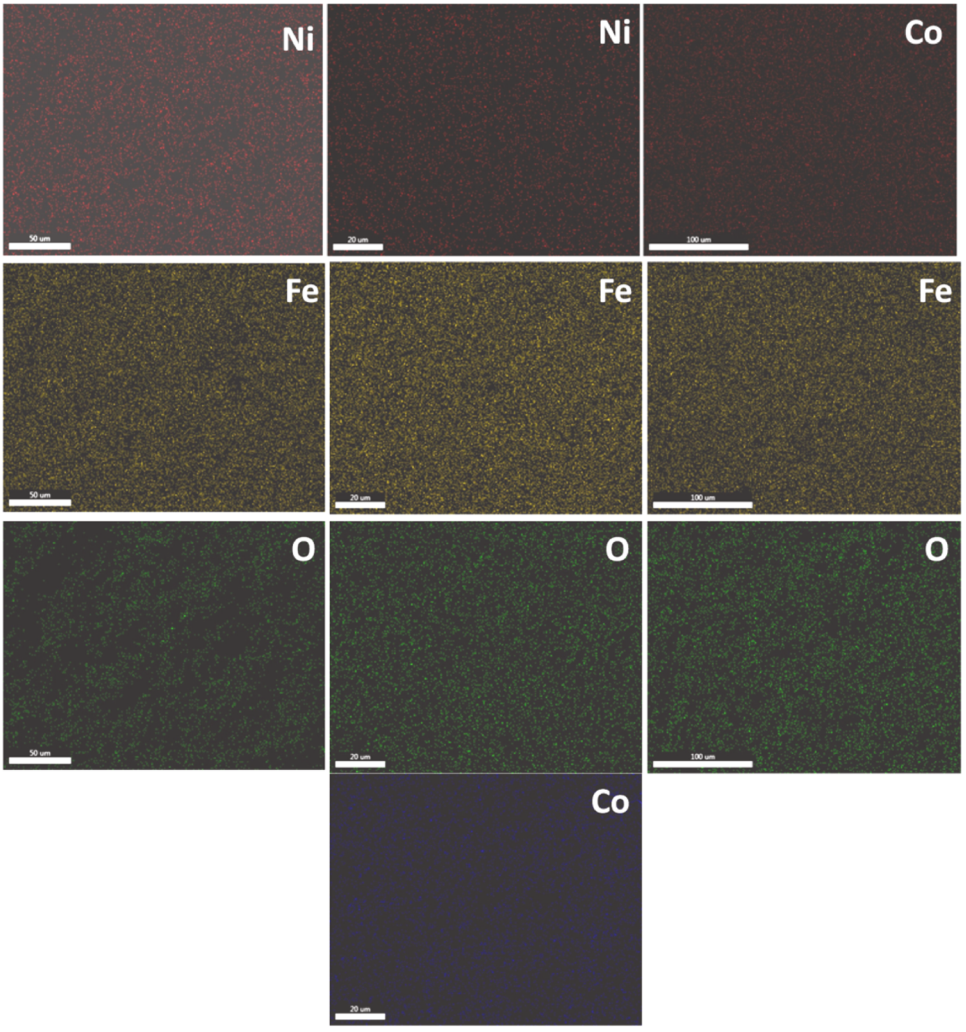

Figure 6. Elemental mapping of (a) $NiFe_2O_4$ (left panel), (b) $Ni_{0.5}Co_{0.5}Fe_2O_4$ (middle panel), and (c) $CoFe_2O_4$ (right panel) sintered samples.

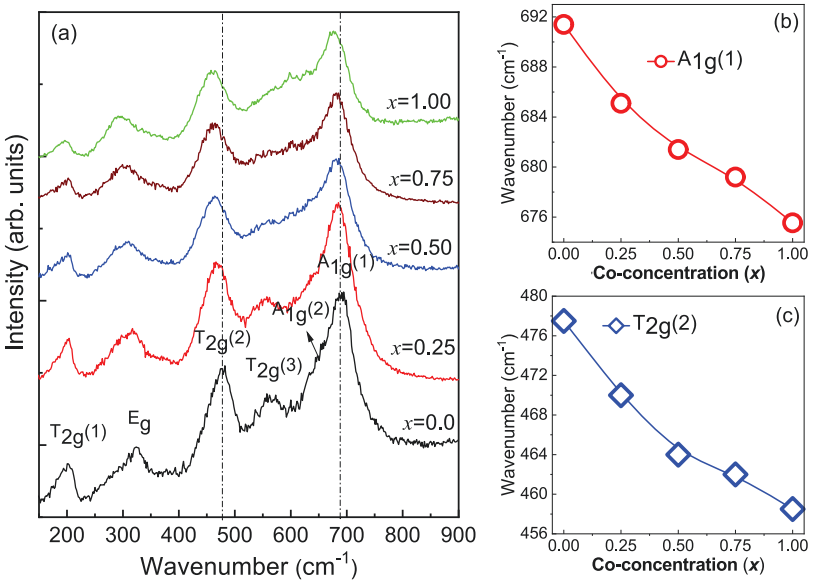

Figure 7. (a) Raman spectra of sintered $Ni_{1-x}Co_xFe_2O_4$ samples recorded at room temperature. (b) and (c) Variation of $A_{1g}(1)$ and $T_{2g}(2)$ band wavenumbers as a function of Co-content in $Ni_{1-x}Co_xFe_2O_4$.

of two other samples. Therefore, in this case, three components were used for deconvolution. The deconvoluted peaks situated at BEs of ~529.24, ~530.92, and ~532.40 eV are attributed to lattice oxygen (O_L, Co/Ni/Fe−O), surface

https://doi.org/10.1021/acsami.2c23025
ACS Appl. Mater. Interfaces 2023, 15, 15691−15706

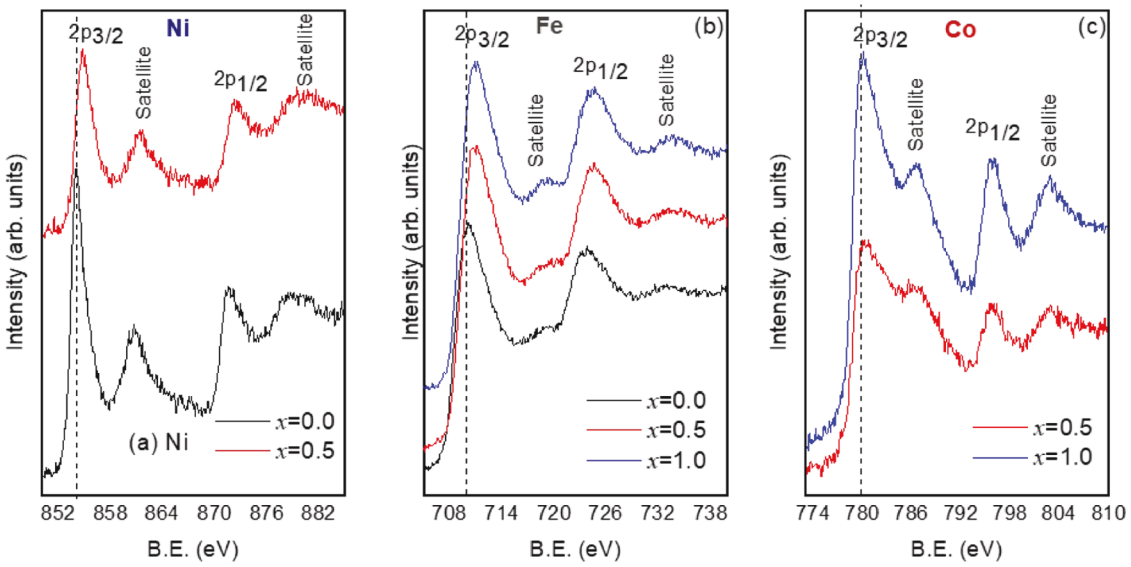

Figure 8. High-resolution XPS spectra of (a) Ni 2p, (b) Fe 2p, and (c) Co 2p core levels in NCFO samples. The peak fitting procedures, respective BE positions, and other XPS parameters (see Tables 2−4) characterize the chemical states of cations as Ni^{2+}, Fe^{3+}, and Co^{2+} in Co-substituted Ni-ferrite.

Table 2. Binding Energies (BEs) of Ni^{2+} Located at Tetrahedral (A-site) and Octahedral (B-site) Sites, Satellite Peaks of $2p_{3/2}$ and $2p_{1/2}$, and BE Difference between $2p_{3/2}$ and $2p_{1/2}$ Peaks for the x = 0 and 0.5 Samples

	Ni $2p_{3/2}$			Ni $2p_{1/2}$		
sample	A-site BE (eV)	B-site BE (eV)	satellite BE (eV)	BE (eV)	satellite BE (eV)	$\Delta(2p_{3/2} - 2p_{1/2})$ (eV)
x = 0.0	854.11	855.82	860.64	872.01	878.44	17.91
x = 0.5	854.67	856.17	861.20	872.62	879.52	17.95

Table 3. Binding Energies (BE) of Fe^{3+} Located at Tetrahedral (A-Site) and Octahedral (B-Site) Sites, Satellite Peaks of $2p_{3/2}$ and $2p_{1/2}$, and BE Difference between $2p_{3/2}$ and $2p_{1/2}$ Peaks for the x = 0.0, 0.5, and 1.0 Samples

	Fe $2p_{3/2}$			Fe $2p_{1/2}$		
sample	A-site BE (eV)	B-site BE (eV)	satellite BE (eV)	BE (eV)	satellite BE (eV)	$\Delta(2p_{3/2} - 2p_{1/2})$ (eV)
x = 0.0	709.79	712.39	717.18	723.80	732.80	13.76
x = 0.5	710.23	712.32		724.10		13.35
x = 1.0	710.27	712.61	718.60	724.10		13.23

Table 4. Binding Energies (BE) of Co^{2+} Located at Tetrahedral (A-Site) and Octahedral (B-Site) Sites, Satellite Peaks of $2p_{3/2}$ and $2p_{1/2}$, and BE Difference between $2p_{3/2}$ and $2p_{1/2}$ Peaks for the x = 0.5 and 1 Samples

	Co $2p_{3/2}$			Co $2p_{1/2}$		
sample	A-site BE (eV)	B-site BE (eV)	satellite BE (eV)	BE (eV)	satellite BE (eV)	$\Delta(2p_{3/2} - 2p_{1/2})$ (eV)
x = 0.5	780.12	782.75	786.64	795.78	802.65	15.66
x = 1.0	779.91	782.32	786.42	795.85	802.79	15.94

Table 5. Cation Distribution of the Samples, as Obtained from XPS Data Analysis

sample	A-site	B-site
$NiFe_2O_4$	$Ni_{0.08}Fe_{0.92}$	$Ni_{0.92}Fe_{1.08}$
$Ni_{0.5}Co_{0.5}Fe_2O_4$	$Ni_{0.04}Co_{0.16}Fe_{0.8}$	$Ni_{0.46}Co_{0.34}Fe_{1.2}$
$CoFe_2O_4$	$Co_{0.35}Fe_{0.65}$	$Co_{0.65}Fe_{1.35}$

hydroxyl (Co/Ni/Fe-OH), and loosely bonded oxygen, mostly adsorbed water molecules or adsorbed O^{2-}, respectively.[17] The BEs of these peaks match well with the reported BEs of oxygen for spinel ferrite systems.[31] The position of the O_L peak is sensitive to samples' heat treatment and chemical doping.[31,34] Unlike the parent sample, for the samples of x = 0.5 and 1.0, a good fit was reached when the O 1s peak was deconvoluted using two components. The positions of the deconvoluted peaks for all of these samples are given in Table 6. It is evident from Table 6 that the BE of O_L increases from 529.24 eV for x = 0 to 529.87 eV for x = 1. The variation in bond length between metal and oxygen (M−O) changes the BEs of lattice oxygen (O_L) in metal oxide ceramic systems.[54−56] The BE increase is mainly due to an increase in the bond length. A longer bond length between the metal and oxygen (M−O) creates less electron density around the nucleus of oxygen, as a result of which more X-ray energy is required to remove the electron from the core−shell, hence increasing the binding energy.[54−56]

https://doi.org/10.1021/acsami.2c23025
ACS Appl. Mater. Interfaces 2023, 15, 15691−15706

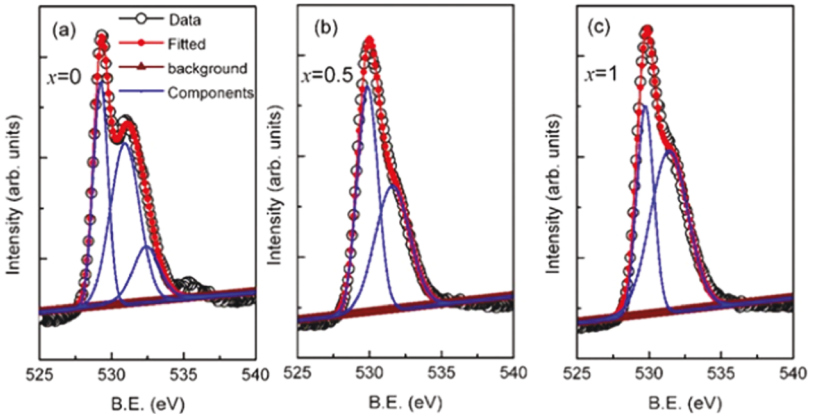

Figure 9. XPS spectra of the O 1s core level in NCFO samples. The deconvoluted peaks located at BEs of ~529.24, ~530.92, and ~532.40 eV are attributed to lattice oxygen (O_L), defective oxygen (O_D), and chemically adsorbed oxygen (O_C), respectively.

Table 6. Binding Energies of O 1s Peaks, Obtained after the Deconvolution

sample	lattice oxygen (O_L) (eV)	defective oxygen (O_D) (eV)	chemical adsorbed oxygen (O_C) (eV)
x = 0.0	529.24	530.92	532.4
x = 0.5	529.74	531.38	
x = 1.0	529.87	531.58	

Magnetic Properties. Hysteresis loops of magnetization versus magnetic field (M *vs* H) for NCFO series measured at room temperature in the magnetic field range of -20 kOe $\leq H \leq +20$ kOe are presented in Figure 10a. The enlarged or zoomed-in magnetization curves of the NCFO samples at low magnetic fields are shown in the inset of Figure 10a. The first-order derivatives of the thermomagnetization (M vs T) curves for the NCFO samples are shown in Figure 10b. These curves allowed us to determine the Curie temperature (T_C) of the samples. All of the magnetic data reveal that the replacement of the low-magnetic cation Ni^{2+} (2 μ_B) by the high-magnetic cation Co^{2+} ($3\mu_B$) in $NiFe_2O_4$ has a profound influence on its magnetic properties. First, it is clear from Figure 10a and the inset that the magnetization (M) and coercivity (H_C) of NCFO series change from a soft-magnetic ferrite phase ($NiFe_2O_4$) to a hard-magnetic ferrite phase ($CoFe_2O_4$) in a systematic manner. Then, the values of the NCFO sample saturation magnetization (M_S) and first-order magnetocrystalline anisotropy constant (K_1) also increase with Co-content. The variations of all of the magnetic parameters are shown in Figure 11. The M_S and K_1 values were extracted using the law of approach to saturation method described in our previous report.[34]

The Co-substitution induced changes in the magnetic parameters, and their dependence on x values enhances our ability to design materials with optimal properties. It is evident (Figure 11a) that M_S increases from 47 to 81 emu/g as the Co^{2+} content increases from 0 to 1. The net effect of increasing Co-concentration and increased M_S is basically due to replacement of the low-magnetic cation Ni^{2+} ($2\mu_B$, d^8 system) by the high-magnetic cation Co^{2+} ($3\mu_B$, d^7 system) at the octahedral sites of the spinel ferrite. In cubic-spinel ferrite systems, magnetization predominantly arises due to a difference in the magnetizations of octahedral (B-site) and tetrahedral (A-site) sites. Thus, when a low-magnetic cation (Ni^{2+} in this case) is substituted by a high-magnetic cation (Co^{2+} in this case) at the octahedral site of the cubic-spinel ferrite, the magnetization of the octahedral site would be higher than that of the tetrahedral site. As a result, the overall magnetization of the doped or substituted sample will be higher than that of the unsubstituted or intrinsic sample.

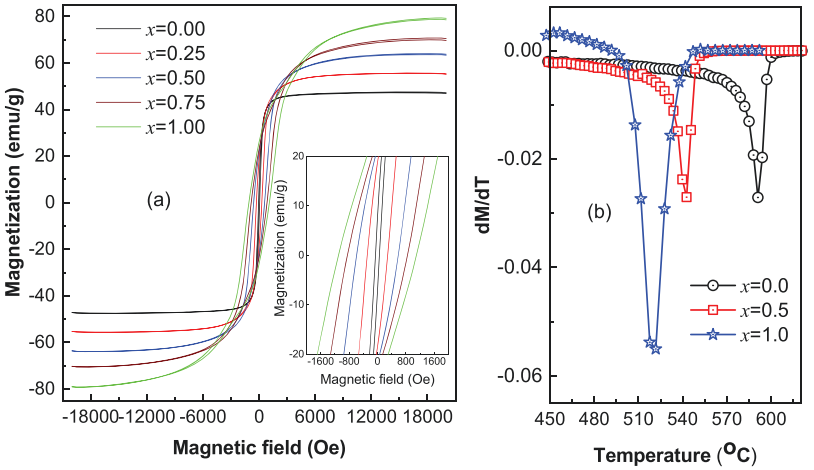

Figure 10. (a) Field-dependent magnetization hysteresis loops of the NCFO samples. Inset of (a) shows zoomed-in hysteresis loops of the samples at a low magnetic field. (b) First-order derivative of thermomagnetization curves as a function of temperature for x = 0.0, 0.5, and 1.0.

https://doi.org/10.1021/acsami.2c23025
ACS Appl. Mater. Interfaces 2023, 15, 15691−15706

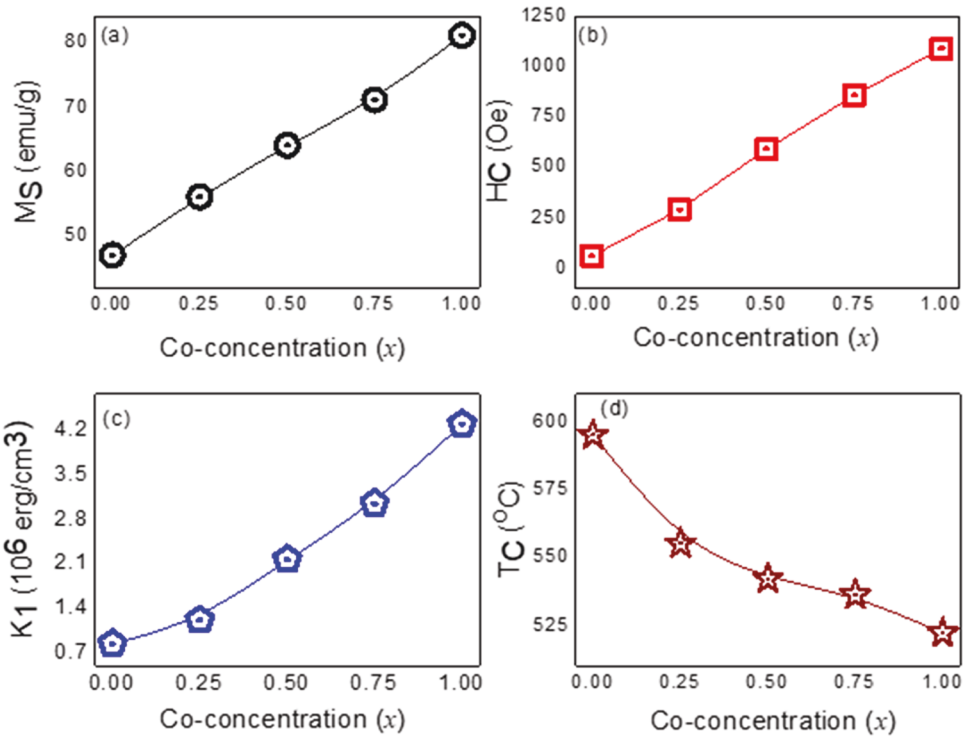

Figure 11. Variation of (a) saturation magnetization (M_S), (b) coercivity (H_C), (c) anisotropy constant (K_1), and (d) Curie temperature (T_C) as a function of cobalt content x in NCFO samples.

Corroborating with XRD results, M_S also increases linearly up to composition $x = 0.5$ and then slightly deviates, most likely as a result of cation redistribution under the influence of increased Co-content starting around $x = 0.5$.

Similar to M_S variation with x, H_C also increases from 57 for $x = 0$ to 1088 Oe for $x = 1$ (see Figure 11b). The microstructural parameters (grain size, grain orientation, density, and porosity), substituent nature, magnetocrystalline anisotropy, and saturation magnetization are known to influence the H_C magnitude in ferrites and their derivatives. Therefore, the variation in microstructural parameters, saturation magnetization, and anisotropy of the samples can be considered to comprehend the variation of H_C with x in NCFO materials. Since H_C is inversely proportional to the ferrite grain size, an increase in grain size should result in a decrease of H_C. However, the H_C value does not decrease as the grain size increases with x, but rather increases with x, indicating that, in the present case, grain size has little effect on H_C values. According to Brown's relation ($H_C = 2K_1/M_S$), H_C is inversely proportional to M_S and directly proportional to K_1. In this work, despite the fact that M_S values rise with x, the increased H_C values are due to the increased magnetocrystalline anisotropy constant. Thus, the increase in H_C with x in NCFO indicates that the K_1 increases at a faster rate than M_S. The K_1 values of NCFO estimated through the LAS method are plotted as a function of x in Figure 11c. As expected, K_1 increases with increasing Co-content, primarily due to replacement of low-anisotropic cations (Ni^{2+}) by high-anisotropic cations (Co^{2+}) at the octahedral sites of the spinel ferrite. The spin−orbit coupling of Co^{2+} is completely responsible for the high anisotropy in Co^{2+}. It is worth mentioning that the percentage of increment in K_1 for change in $x = 0$−0.5 is 157%, which is significantly higher than the percentage of increment in M_S (36%). In other words, the rate of increase in K_1 is higher than that observed for the M_S values and accounts for the observed enhancement in H_C.

Measuring the Curie temperature (T_C) helps us understand the magnetic exchange strength (A−O−B superexchange interactions) between the cations are located at the octahedral and tetrahedral sites of the spinel-type ferrites. A nonlinear decrease in T_C from 595 °C for $x = 0$ to 522 °C for $x = 1$ is seen in Figure 11d. The T_C values of $NiFe_2O_4$ ($x = 0$) and $CoFe_2O_4$ ($x = 1$) in the present study are in agreement with the values reported in the literature.[16,34] The nonlinear variation is most probably due to the effect of cation distribution between A- and B-sites. Commonly, when a magnetic cation of the spinel-type ferrite system is replaced by a nonmagnetic cation such as Mg^{2+}, Zn^{2+}, Al^{3+}, Ga^{3+}, In^{3+}, etc., the T_C of the ferrite system decreases due to the absence of magnetic interactions between magnetic and nonmagnetic cations.[16] In the present study, replacing a low-magnetic cation (Ni^{2+}) by a high-magnetic cation (Co^{2+}) at the octahedral sites increased the A-O-B magnetic exchange strength, and, as a result of that, T_C should also increase with increasing Co^{2+} content. However, the decrease in T_C with x increasing can be described on the basis of bond length increase.[16] T_C of the spinel-type ferrite systems depends not only on the strength of magnetic exchange interactions between the magnetic cations mediated through oxygen but also on how far the magnetic cations located away from the oxygen. If the magnetic cations are far from the oxygen, then the magnetic interactions between the cations through oxygen would be lesser, which leads to lowering of T_C. As revealed from XRD and Raman analyses, there is an increase in bond length upon Co-substitution. The increased bond length lowers the magnetic exchange strength and thus decreases T_C with the increase in Co^{2+} content in NCFO.

https://doi.org/10.1021/acsami.2c23025
ACS Appl. Mater. Interfaces 2023, 15, 15691−15706

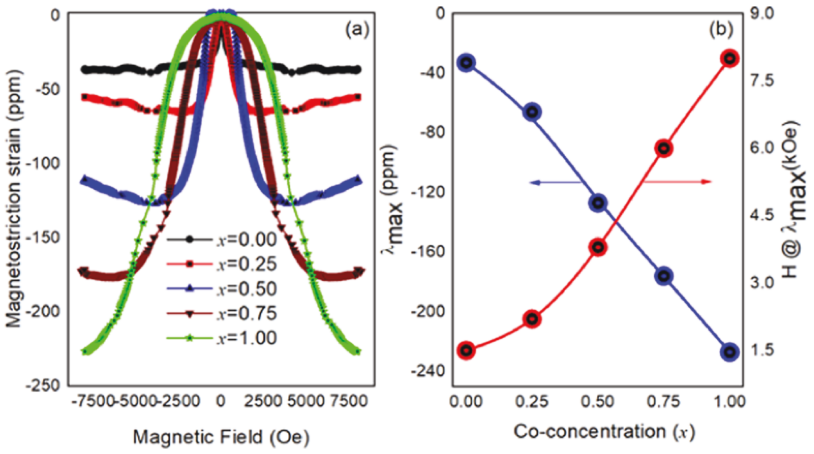

Figure 12. (a) Room-temperature magnetostriction strain curves measured as a function of the magnetic field applied along the parallel direction ($\lambda_{\parallel}$) for the NCFO series of samples. (b) Variation of λ_{max} (left arrow) and the field (H) at which λ_{max} obtained (right arrow) as a function of x.

Magnetostriction Studies. Room-temperature magnetostriction strains (λ), which are measured by applying a magnetic field (-8 kOe $\leq H \leq +8$ kOe) parallel to the axis of a strain gauge cemented on a disc-shaped NCFO pellet, are shown in Figure 12a. Similar to magnetic parameters, incorporation of Co^{2+} into the Ni-ferrite lattice has a profound impact on the magnetostriction strain values. The -33 ppm is the maximum magnetostriction strain (λ_{max}) determined for intrinsic NFO ($x = 0$) at an applied magnetic field of 1.4 kOe. This value is comparable to the magnetostriction strain values frequently reported for the $NiFe_2O_4$ systems.[57,58] The remarkable effect of Co^{2+} content in NCFO is seen in terms of significant changes in the shape of the magnetostriction strain curves. Initially, the λ_{max} increases approximately linearly from the value -33 ppm ($x = 0$) to -227 ppm for $x = 1$ ($CoFe_2O_4$), along with the magnitude of the magnetic field where the λ_{max} occurs (see Figure 12b). $CoFe_2O_4$ did not reach saturation, unlike $NiFe_2O_4$, even at 8 kOe (the highest measuring field of the magnetostriction equipment), indicating that a higher magnetostriction can be expected for $CoFe_2O_4$ even at higher magnetic fields (H > 8 kOe). The possible reason for not attaining saturation magnetostriction in the $x = 1$ ($CoFe_2O_4$) sample is due to the higher coercivity and magnetocrystalline anisotropy associated with its smaller grains. The linear increase in λ_{max} with x is predominantly due to the increase in the Co^{2+} concentration at the spinel ferrite's octahedral coordination sites (B-sites). Due to the high magnetostriction found in Co-substituted NFO, the samples' magnetocrystalline anisotropy is enhanced by the strong spin–orbit coupling of Co^{2+} at the octahedral sites. In the literature reports, it was shown that the ferrite magnetostriction magnitude is also influenced by the microstructure. However, the microstructure plays a minor role in this study even though the grain size increased with the Co-content x. The increase in the magnetic field at which λ_{max} was obtained for different Co-substituted compositions is due to the hard-magnetic and high-anisotropic nature of the samples, as revealed from the magnetization data analysis.

Two evidently distinguishable slopes, a negative slope at low magnetic fields and a positive slope at high magnetic fields, in the magnetostriction strain curve are observed for the intermediate composition $x = 0.5$. The major negative slope at low fields arises from λ_{100} (magnetostriction coefficient along the 100 crystallographic direction), whereas the minor positive slope at high fields is due to λ_{111} (magnetostriction coefficient along the [111] crystallographic direction).[32,53] Among all of the NCFO materials, the $x = 0.5$ sample demonstrates better magnetostriction in the magnetic field region of 1 kOe $\leq H \leq$ 2 kOe owing to its low anisotropy than that of the $CoFe_2O_4$ sample. The NCFO materials with x=0.25 and 0.50 are likely to be suitable for low-field magnetostrictive device applications due to their high magnetostriction at low fields, whereas the $x = 0.75$ and 1.00 compositions can be suitable for high-field magnetostrictive device applications due to their high magnetostriction at higher magnetic fields.

Strain sensitivity ($d\lambda/dH$), the first-order derivative of the magnetostriction strain curve, is another vital parameter of magnetostrictive materials that projects the suitability of the material for potential sensor applications. For industrial applications, particularly for sensor-related applications, materials with high-strain sensitivity at low fields are desirable. In Figure 13, we show the variation of maximum strain sensitivity $[d\lambda/dH]_{max}$ as a function of Co-concentration. Again, among all compositions, -2.3×10^{-9} m/A is the highest $[d\lambda/dH]_{max}$ obtained for $x = 0.5$. Although λ_{max} of the $CoFe_2O_4$ ($x = 1$) sample is higher at a higher magnetic field

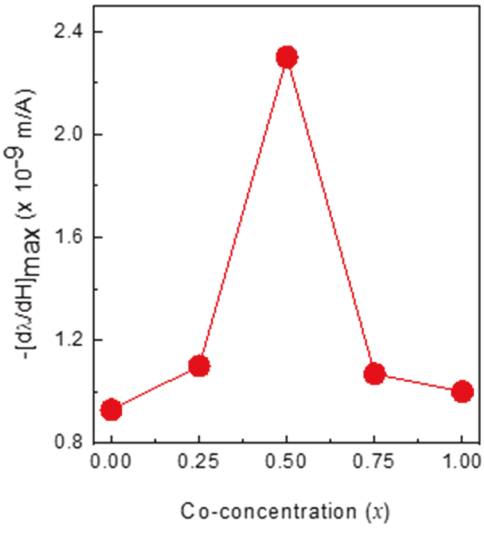

Figure 13. Variation of maximum strain sensitivity $[d\lambda/dH]_{max}$ as a function of Co-content (x) in NCFO samples.

https://doi.org/10.1021/acsami.2c23025
ACS Appl. Mater. Interfaces 2023, 15, 15691−15706

Table 7. Comparison of Magnetostriction Parameters of Reported Metal-Substituted Nickel Ferrite and the Results in the Present Study

sample	synthesis method	sintering temperature and time	λ_{max} (ppm)	field @ λ_{max} (kA/m)	$(d\lambda/dH)_{max} \times 10^{-9}$ m/A	ref
$Ni_{0.5}Co_{0.5}Fe_2O_4$	sol−gel	1200 °C, 4 h	−63	119	−1.74	58
$Co_{0.6}Ni_{0.4}Fe_2O_4$	coprecipitation	600 °C, 8 h	−35	477	NP	25
$Co_{0.5}Ni_{0.5}Fe_2O_4$	solid state	1500 °C, 10 min	−114	308	NP	33
$Co_{0.9}Ni_{0.1}Fe_2O_4$	solid state	1450 °C, 10 min	−186	308	−0.67	60
$Ni_{0.75}Zn_{0.25}Fe_2O_4$	sol−gel	1200 °C, 12 h	−20	400	−0.238	32
$Ni_{0.5}Zn_{0.5}Fe_2O_4$			−8	398	−0.2	
$Zn_{0.35}Ni_{0.65}Fe_2O_4$	sol−gel	350 °C, 4 h	−10	398	NP	57
$Zn_{0.25}Ni_{0.75}Fe_2O_4$			−30	318		
$Co_{0.9}Ni_{0.1}Fe_2O_4$	coprecipitation	600 °C, 20 min	−180	318	−1.4	35
$NiFe_{1.925}Sm_{0.075}O_4$	solid state	1250 °C, 12 h	−34	438	NP	18
$NiFe_{1.925}Ho_{0.075}O_4$			−24	298		
$Ni_{0.6}Zn_{0.4}Fe_{1.5}Al_{0.5}O_4$	sol−gel	1200 °C, 24 h	−10	80	NP	61
$Ni_{0.5}Co_{0.5}Fe_2O_4$	autocombustion	1200 °C, 2 h	−160	316	−2.3	[a]

[a]Present work; NP, not presented/reported and/or not available.

and that of $NiFe_2O_4$ ($x = 0$) is lower at a lower magnetic field, both samples exhibit almost the same value of $[d\lambda/dH]_{max}$ ($\sim -0.9 \times 10^{-9}$ m/A). In fact, the $[d\lambda/dH]_{max}$ of $CoFe_2O_4$ in the present study is relatively lower than the values often reported for sintered Co-ferrite systems,[19,59] possibly due to differences in processing conditions and microstructure of the materials. Higher λ_{max} relatively at a lower magnetic field is a critical requirement to accomplish higher strain sensitivity in the magnetostrictive materials for sensors. For instance, the λ_{max} of the composition with $x = 0.5$ is lower than that of the $x = 1$ sample, but the field at λ_{max} obtained for the sample is remarkably lower than that of the $x = 1$ sample, and hence the higher strain sensitivity for the $x = 0.5$ sample. On the other hand, even though the λ_{max} of the $x = 0.25$ sample was obtained at a lower magnetic field compared to the $x = 0.5$ sample, this value is not adequate to have a higher strain sensitivity. Based on the magnetostriction studies, we believe that the composition with $x = 0.5$ would be a suitable material against Ni- and Co-ferrites due to its higher λ_{max} and $[d\lambda/dH]_{max}$.

In Table 7, the magnetostriction parameters (λ_{max} and $[d\lambda/dH]_{max}$) obtained for our material ($Ni_{0.5}Co_{0.5}Fe_2O_4$) are compared with the reported values for various metal-substituted NFO samples prepared from different methods and/or processed under different conditions. As is evident from the table, the λ_{max} and $[d\lambda/dH]_{max}$ magnitudes depend greatly on the synthesis method and processing conditions. Among all of the reported materials of doped NFO, the $Ni_{0.5}Co_{0.5}Fe_2O_4$ sample, fabricated in this work, shows a higher $[d\lambda/dH]_{max}$, even at a lower magnetic field. Among all of the reported metal-substituted nickel ferrite samples, the highest strain sensitivity (-2.3×10^{-9} m/A) is obtained in this work for $Ni_{1-x}Co_xFe_2O_4$ ($x = 0.5$), which is thus the optimum composition for sensor applications.

SUMMARY AND CONCLUSIONS

This study reveals that replacing Ni^{2+} with Co^{2+} has a significant impact on the structural, microstructural, magnetic, and magnetostrictive properties of $NiFe_2O_4$. Due to the substitution of a larger cation (Co^{2+}) for a smaller cation (Ni^{2+}) in the spinel ferrite lattice structure, lattice expansion occurs. The lattice constant increase from 8.3268 Å ($x = 0$) to 8.3751 Å ($x = 1$) is the remarkable effect of Co-substitution in NFO. As the cobalt content in the spinel Ni-ferrite increases, so does the Ni-ferrite grain size, as seen in SEM images of the Co-substituted NCFO materials. The effects of Co^{2+} substitution on the structural parameters (bond length, etc.) were also revealed by Raman spectroscopic analyses, which are in perfect agreement and corroborate XRD and SEM results and analyses. Chemical quality assessment by EDS and XPS analyses confirms the chemical homogeneity and uniform distribution of Co, Ni, Fe, and O in all of the samples, while XPS validates the existence of cations in their respective chemical states of Co^{2+}, Ni^{2+}, and Fe^{3+}. In the NCFO series of compounds, the substitution of the low-magnetic and anisotropic cation (Ni^{2+}, $2\mu_B$) by the high-magnetic and anisotropic cation (Co^{2+}, $3\mu_B$) at the octahedral sites of the spinel Ni-ferrite increases all of the magnetic parameters (M_S, H_C, K_1), with the exception of T_C. The soft magnetic phase ($NiFe_2O_4$, when $x = 0$) gradually transforms into the hard magnetic phase ($CoFe_2O_4$, when $x = 1$) as the Co^{2+} content increases. The decrease in T_C with Co-content x can be attributed to the drop in the magnetic exchange strengths between the magnetic cations through oxygen (M−O−M) due to the increase in the M−O bond lengths. The increasing Co-content in NCFO series results in almost a linear increase in the maximum magnetostriction strain (λ_{max}) along with the field at which λ_{max} is obtained. The strong spin−orbit coupling of Co^{2+} ions located at the octahedral sites is responsible for the linear increase in λ_{max}. Toward sensor applications, optimization of the materials and a parametric study reveal that the NCFO composition $x = 0.5$ ($Ni_{0.5}Co_{0.5}Fe_2O_4$) has maximum strain sensitivity ($[d\lambda/dH]_{max}$, -2.3×10^{-9} m/A) against other compositions in $Ni_{1-x}Co_xFe_2O_4$. Based on analyses of structural, chemical bonding, magnetic, and magnetostriction results, we conclude that the intermediate composition, particularly $Ni_{0.5}Co_{0.5}Fe_2O_4$, will be an ideal choice for sensor applications over intrinsic Ni- and/or Co-ferrites due to its relatively soft magnetic feature, high magnetostriction strain, and strain sensitivity at low magnetic fields.

ASSOCIATED CONTENT

Supporting Information

The Supporting Information is available free of charge at https://pubs.acs.org/doi/10.1021/acsami.2c23025.

Additional details of grain size histograms, XPS survey scans, and core-level deconvolution procedures and data

https://doi.org/10.1021/acsami.2c23025
ACS Appl. Mater. Interfaces 2023, 15, 15691−15706

analyses of Ni 2p, Fe 2p, and Co 2p core-level XPS peaks (PDF)

AUTHOR INFORMATION

Corresponding Authors

Pendaranahalli Nadikeraiah Anantharamaiah − *Department of Chemistry, Faculty of Mathematical and Physical Sciences, M. S. Ramaiah University of Applied Sciences, Bangalore 560058, India;* orcid.org/0000-0001-8919-3686; Email: anantharamaiah.cy.mp@msruas.ac.in

C. V. Ramana − *Center for Advanced Materials Research and Department of Aerospace & Mechanical Engineering, University of Texas at El Paso, El Paso, Texas 79968, United States;* orcid.org/0000-0002-5286-3065; Email: rvchintalapalle@utep.edu

Authors

Mudalagiriyappa Satish − *Department of Chemistry, Faculty of Mathematical and Physical Sciences, M. S. Ramaiah University of Applied Sciences, Bangalore 560058, India*

Hadonahalli Munegowda Shashanka − *Department of Chemistry, Faculty of Mathematical and Physical Sciences, M. S. Ramaiah University of Applied Sciences, Bangalore 560058, India*

Sujoy Saha − *Materials Research Centre, Indian Institute of Science, Bangalore 560012, India*

Keerthi Haritha − *Environmental Science and Engineering, University of Texas at El Paso, El Paso, Texas 79968, United States*

Debabrata Das − *Center for Advanced Materials Research and Department of Aerospace & Mechanical Engineering, University of Texas at El Paso, El Paso, Texas 79968, United States;* orcid.org/0000-0003-4326-6805

Complete contact information is available at: https://pubs.acs.org/10.1021/acsami.2c23025

Notes

The authors declare no competing financial interest.

ACKNOWLEDGMENTS

P.N.A. is grateful to the SERB/DST, Govt. of India, for the financial support through the sanction order number CRG/2018/002925. C.V.R. acknowledges, with pleasure, support from the National Science Foundation (NSF) with NSF-PREM grant #DMR-1827745.

REFERENCES

(1) Ge, M.; Xu, D.; Chen, Z.; Wei, C.; Zhang, Y.; Yang, C.; Chen, Y.; Lin, H.; Shi, J. Magnetostrictive-Piezoelectric-Triggered Nanocatalytic Tumor Therapy. *Nano Lett.* **2021**, *21*, 6764−6772.

(2) Head, J.; Manuel, P.; Orlandi, F.; Jeong, M.; Lees, M. R.; Li, R.; Greaves, C. Structural, Magnetic, Magnetocaloric, and Magnetostrictive Properties of $Pb_{1-x}Sr_xMnBO_4$ (x = 0, 0.5, and 1.0). *Chem. Mater.* **2020**, *32*, 10184−10199.

(3) Anantharamaiah, P. N.; Shashanka, H. M.; Srinivasan, S.; Das, D.; El-Gendy, A. A.; Ramana, C. V. Structural, Magnetic, and Magnetostriction Properties of Flexible, Nanocrystalline $CoFe_2O_4$ Films Made by Chemical Processing. *ACS Omega* **2022**, *7*, 43813−43819.

(4) Narita, F.; Fox, M. A Review on Piezoelectric, Magnetostrictive, and Magnetoelectric Materials and Device Technologies for Energy Harvesting Applications. *Adv. Eng. Mater.* **2018**, *20*, No. 1700743.

(5) Joy, B.; Cai, Y.; Bono, D. C.; Sarkar, D. Cell Rover—A Miniaturized Magnetostrictive Antenna for Wireless Operation Inside Living Cells. *Nat. Commun.* **2022**, *13*, No. 5210.

(6) Jiang, S.; Xie, H.; Shan, J.; Mak, K. F. Exchange Magnetostriction in Two-Dimensional Antiferromagnets. *Nat. Mater.* **2020**, *19*, 1295−1299.

(7) Zhao, Z.; Sui, X. Temperature Compensation Design and Experiment for a Giant Magnetostrictive Actuator. *Sci. Rep.* **2021**, *11*, No. 251.

(8) Spizzo, F.; Greco, G.; Del Bianco, L.; Coïsson, M.; Pugno, N. M. Magnetostrictive and Electroconductive Stress-Sensitive Functional Spider Silk. *Adv. Funct. Mater.* **2022**, *32*, No. 2207382.

(9) Pashchenko, A. V.; Liedienov, N. A.; Fesych, I. V.; Li, Q.; Pitsyuga, V. G.; Turchenko, V. A.; Pogrebnyak, V. G.; Liu, B.; Levchenko, G. G. Smart Magnetic Nanopowder Based on the Manganite Perovskite for Local Hyperthermia. *RSC Adv.* **2020**, *10*, 30907−30916.

(10) Gao, C.; Zeng, Z.; Peng, S.; Shuai, C. Magnetostrictive Alloys: Promising Materials for Biomedical Applications. *Bioact. Mater.* **2022**, *8*, 177−195.

(11) Engdahl, G. *Handbook of Giant Magnetostriction Materials*; Academic Press: San Diego, 2000.

(12) Estrine, E. C.; Robbins, W. P.; Maqableh, M. M.; Stadler, B. J. Electrodeposition and Characterization of Magnetostrictive Galfenol (FeGa) Thin Films for Use in Microelectromechanical Systems. *J. Appl. Phys.* **2013**, *113*, No. 17A937.

(13) Keswani, B. C.; Patil, S. I.; Kolekar, Y. D.; Ramana, C. V. Improved Magnetostrictive Properties of Cobalt Ferrite ($CoFe_2O_4$) by Mn and Dy Co-Substitution for Magneto-Mechanical Sensors. *J. Appl. Phys.* **2019**, *126*, No. 174503.

(14) Orozco, C.; Melendez, A.; Manadhar, S.; Singamaneni, S. R.; Reddy, K. M.; Gandha, K.; Niebedim, I. C.; Ramana, C. V. Effect of Molybdenum Incorporation on the Structure and Magnetic Properties of Cobalt Ferrite. *J. Phys. Chem. C* **2017**, *121*, 25463−25471.

(15) Kulandaivel, A.; Jawaharlal, H. Extensive Analysis on the Thermoelectric Properties of Aqueous Zn-Doped Nickel Ferrite Nanofluids for Magnetically Tuned Thermoelectric Applications. *ACS Appl. Mater. Interfaces* **2022**, *14*, 26833−26845.

(16) Anantharamaiah, P. N.; Joy, P. A. Effect of Size and Site Preference of Trivalent Non-Magnetic Metal ions (Al^{3+}, Ga^{3+}, In^{3+}) Substituted for Fe^{3+} on the Magnetostrictive Properties of Sintered $CoFe_2O_4$. *J. Phys. D* **2017**, *50*, No. 435005.

(17) Ortiz-Quiñonez, J.-L.; Pal, U.; Villanueva, M. S. Structural, Magnetic, and Catalytic Evaluation of Spinel Co, Ni, and Co-Ni Ferrite Nanoparticles Fabricated by Low-Temperature Solution Combustion Process. *ACS Omega* **2018**, *3*, 14986−15001.

(18) Bharathi, K. K.; Markandeyulu, G.; Ramana, C. V. Structural, Magnetic, Electrical, and Magnetoelectric Properties of Sm- and Ho-Substituted Nickel Ferrites. *J. Phys. Chem. C* **2011**, *115*, 554−560.

(19) Nlebedim, I. C.; Ranvah, N.; Williams, P. I.; Melikhov, Y.; Anayi, F.; Snyder, J. E.; Moses, A. J.; Jiles, D. C. Influence of Vacuum Sintering on Microstructure and Magnetic Properties of Magnetostrictive Cobalt Ferrite. *J. Magn. Magn. Mater.* **2009**, *321*, 2528−2532.

(20) Abramovich, A. I.; Michurin, A. V. Giant Volume Magnetostriction in CMR Manganites $R_{1-x}Sr_xMnO_3$ (R=Sm, Nd). *Low. Temp. Phys.* **2001**, *27*, 278−282.

(21) Koroleva, L. I.; Demin, R. V.; Kozlov, A. V.; Zashcherinskii, D. M.; Gorbenko, O. Y.; Kaul, A. R.; Melnikov, O. V.; Mukovskii, Y. M. Giant Volume Magnetostriction and its Connection with Colossal Magnetoresistance and Lattice-Softening $La_{1-x}M_xMnO_3$ (M=Ca, Ag, Ba, Sr). *J. Magn. Magn. Mater.* **2007**, *316*, e644−e647.

(22) Ansari, S. M.; Sinha, B. B.; Phase, D.; Sen, D.; Sastry, P. U.; Kolekar, Y. D.; Ramana, C. V. Particle Size, Morphology, and Chemical Composition Controlled $CoFe_2O_4$ Nanoparticles with Tunable Magnetic Properties via Oleic Acid Based Solvothermal Synthesis for Application in Electronic Devices. *ACS Appl. Nano Mater.* **2019**, *2*, 1828−1843.

(23) Kharat, S. P.; Gaikwad, S. K.; Kambale, R. C.; Kolekar, Y. D.; Ramana, C. V. Correlation between Cation Distribution and Magnetic

and Dielectric Properties of Dy^{3+}-Substituted Fe-Rich Cobalt Ferrite. *Inorg. Chem.* **2022**, *61*, 19319−19332.
(24) Kamala Bharathi, K.; Balamurugan, K.; Santhosh, P. N.; Pattabiraman, M.; Markandeyulu, G. Magnetocapacitance in Dy-Doped Ni Ferrite. *Phys. Rev. B* **2008**, *77*, No. 172401.
(25) Mathe, V. L.; Sheikh, A. D. Magnetostrictive Properties of Nanocrystalline Co−Ni Ferrites. *Phys. B* **2010**, *405*, 3594−3598.
(26) Demirci Dönmez, Ç. E.; Manna, P. K.; Nickel, R.; Aktürk, S.; van Lierop, J. Comparative Heating Efficiency of Cobalt-, Manganese-, and Nickel-Ferrite Nanoparticles for a Hyperthermia Agent in Biomedicines. *ACS Appl. Mater. Interfaces* **2019**, *11*, 6858−6866.
(27) Albino, M.; Fantechi, E.; Innocenti, C.; López-Ortega, A.; Bonanni, V.; Campo, G.; Pineider, F.; Gurioli, M.; Arosio, P.; Orlando, T.; Bertoni, G.; de Julián Fernández, C.; Lascialfari, A.; Sangregorio, C. Role of Zn^{2+} Substitution on the Magnetic, Hyperthermic, and Relaxometric Properties of Cobalt Ferrite Nanoparticles. *J. Phys. Chem. C* **2019**, *123*, 6148−6157.
(28) Debnath, B.; Salunke, H. G.; Bhattacharyya, S. Spin Disorder and Particle Size Effects in Cobalt Ferrite Nanoparticles with Unidirectional Anisotropy and Permanent Magnet-like Characteristics. *J. Phys. Chem. C* **2020**, *124*, 25992−26000.
(29) Shirsath, S. E.; Wang, D.; Zhang, J.; Morisako, A.; Li, S.; Liu, X. Single-Crystal-like Textured Growth of $CoFe_2O_4$ Thin Film on an Amorphous Substrate: A Self-Bilayer Approach. *ACS Appl. Electron. Mater.* **2020**, *2*, 3650−3657.
(30) Shirsath, S. E.; Liu, X.; Assadi, M. H. N.; Younis, A.; Yasukawa, Y.; Karan, S. K.; Zhang, J.; Kim, J.; Wang, D.; Morisako, A.; Yamauchi, Y.; Li, S. Au Quantum Dots Engineered Room Temperature Crystallization and Magnetic Anisotropy in $CoFe_2O_4$ Thin Films. *Nanoscale Horiz.* **2019**, *4*, 434−444.
(31) Shirsath, S. E.; Liu, X.; Yasukawa, Y.; Li, S.; Morisako, A. Switching of Magnetic Easy-Axis Using Crystal Orientation for Large Perpendicular Coercivity in $CoFe_2O_4$ Thin Film. *Sci. Rep.* **2016**, *6*, No. 30074.
(32) Atif, M.; Nadeem, M.; Grössinger, R.; Turtelli, R. S. Studies on the magnetic, magnetostrictive and electrical properties of sol−gel synthesized Zn doped nickel ferrite. *J. Alloys Compd.* **2011**, *509*, 5720−5724.
(33) Bhame, S. D.; Shirolkar, M. M.; Joy, P. A. Magnetic and Magnetoelastic Properties of Ni-Substituted Cobalt Ferrite. *IEEE Magn. Lett.* **2021**, *12*, 1−5.
(34) Anantharamaiah, P. N.; Rao, B. P.; Shashanka, H. M.; Chelvane, J. A.; Khopkar, V.; Sahoo, B. Role of Mg^{2+} and In^{3+} Substitution on Magnetic, Magnetostrictive and Dielectric Properties of $NiFe_2O_4$ Ceramics Derived from Nanopowders. *Phys. Chem. Chem. Phys.* **2021**, *23*, 1694−1705.
(35) Mane, S. M.; Teli, A. M.; Tayade, N. T.; Pawar, K. J.; Kulkarni, S. B.; Choi, J.; Yoo, J. W.; Shin, J. C. Correlative Structural Refinement-Magnetic Tunability, and Enhanced Magnetostriction in Low-Temperature, Microwave-Annealed, Ni-Substituted $CoFe_2O_4$ Nanoparticles. *J. Alloys Compd.* **2022**, *895*, No. 162627.
(36) Phugate, D. V.; Brade, R. B.; Kadam, S. B.; Dhale, L. A.; Shirsath, S. E.; Kadam, A. B. Effect of Ho^{3+} Ion Doping On Thermal, Structural, Morphological, Properties of Co-Ni Ferrite Synthesized by Sol-Gel Method. *J. Supercond. Novel Magn.* **2020**, *33*, 3545−3554.
(37) Almessiere, M. A.; Slimani, Y.; Auwal, I. A.; Shirsath, S. E.; Manikandan, A.; Baykal, A.; Ozcelik, B.; Ercan, I.; Trukhanov, S. V.; Vinnik, D. A.; Trukhanov, A. V. Impact of Tm^{3+} and Tb^{3+} Rare Earth Cations Substitution on the Structure and Magnetic Parameters of Co-Ni Nanospinel Ferrite. *Nanomaterials* **2020**, *10*, 2384.
(38) Hajalilou, A.; Mazlan, S. M. A Review on Preparation Techniques for Synthesis of Nanocrystalline Soft Magnetic Ferrites and Investigation on the Effects of Microstructure Features on Magnetic Properties. *Appl. Phys. A: Mater. Sci. Process.* **2016**, *122*, No. 680.
(39) Soufi, A.; Hajjaoui, H.; Elmoubarki, R.; Abdennouri, M.; Quorzal, S.; Barka, N. Spinel Ferrites Nanoparticles: Synthesis Methods and Applications in Heterogeneous Fenton Oxidation of Organic Pollutants − A Review. *Appl. Surf. Sci. Adv.* **2021**, *6*, No. 100145.
(40) Anantharamaiah, P. N.; Shashanka, H. M.; Saha, S.; Chelvane, J. A.; Sahoo, B. Enabling Cobalt Ferrite ($CoFe_2O_4$) for Low Magnetic Field Strain Responsivity Through Bi^{3+} Substitution: Material for Magnetostrictive Sensors. *J. Alloys Compd.* **2021**, *877*, No. 160285.
(41) *ASTM 10-325 (Ni-ferrite)*; National Bureau of Standards: USA, 1960; 539−1044.
(42) Borah, R.; Ravi, S. Effect of Cation Distributions on Structural and Magnetic Properties of $Ni_{1-x}Co_xFe_2O_4$ Spinel Ferrites. *J. Magn. Magn. Mater.* **2021**, *538*, No. 168276.
(43) Kalidindi, N. R.; Manciu, F. S.; Ramana, C. V. Crystal Structure, Phase, and Electrical Conductivity of Nanocrystalline $W_{0.95}Ti_{0.05}O_3$ Thin Films. *ACS Appl. Mater. Interfaces* **2011**, *3*, 863−868.
(44) Hussain, O. M.; Srinivasa Rao, K.; Madhuri, K. V.; Ramana, C. V.; Naidu, B. S.; Pai, S.; John, J.; Pinto, R. Growth and Characteristics of Reactive Pulsed Laser Deposited Molybdenum Trioxide Thin Films. *Appl. Phys. A* **2002**, *75*, 417−422.
(45) Saini, S.; Yadav, K. L.; Shah, J.; Kotnala, R. K. Enhanced Water Splitting by Strained Lithium-Substituted Nickel Ferrite Hydroelectric Cells. *ACS Appl. Energy Mater.* **2022**, *5*, 8178−8188.
(46) Anantharamaiah, P. N.; Joy, P. A. Tuning of the Magnetostrictive Properties of Cobalt Ferrite by Forced Distribution of Substituted Divalent Metal ions at Different Crystallographic Sites. *J. Appl. Phys.* **2017**, *121*, No. 093904.
(47) Puli, V. S.; Adireddy, S.; Ramana, C. V. Chemical Bonding and Magnetic Properties of Gadolinium (Gd) Substituted Cobalt Ferrite. *J. Alloys Compd.* **2015**, *644*, 470−475.
(48) Hua, M.; Xu, L.; Cui, F.; Lian, J.; Huang, Y.; Bao, J.; Qiu, J.; Xu, Y.; Xu, H.; Zhao, Y.; Li, H. Hexamethylenetetramine-Assisted Hydrothermal Synthesis of Octahedral Nickel Ferrite Oxide Nanocrystallines with Excellent Supercapacitive Performance. *J. Mater. Sci.* **2018**, *53*, 7621−7636.
(49) Ramana, C. V.; Roy, S.; Zade, V.; Battu, A. K.; Makeswaran, N.; Shutthanandan, V. Electronic Structure and Chemical Bonding in Transition-Metal-Mixed Gallium Oxide (Ga_2O_3) Compounds. *J. Phys. Chem. Solids* **2021**, *157*, No. 110174.
(50) Atuchin, V. V.; Vinnik, D. A.; Gavrilova, T. A.; Gudkova, S. A.; Isaenko, L. I.; Jiang, X.; Pokrovsky, L. D.; Prosvirin, I. P.; Mashkovtseva, L. S.; Lin, Z. Flux Crystal Growth and the Electronic Structure of BaFeO Hexaferrite. *J. Phys. Chem. C* **2016**, *120*, 5114−5123.
(51) Feng, G.; Hu, B.; Liu, X.; Wei, Y.; Li, Z.; He, P.; Cheng, Z.; Wang, Y.; Deng, D.; Yang, X. Laser-Induced Exothermic Bonding of SiCp/Al Composites with Nanostructured Al/Ni Energetic Interlayer. *Crystals* **2022**, *12*, 938.
(52) Chimitova, O. D.; Bazarov, B. G.; Bazarova, J. G.; Atuchin, V. V.; Azmi, R.; Sarapulova, A. E.; Mikhailova, D.; Balachandran, G.; Fiedler, A.; Geckle, U.; Prots, Yu.; Komarek, A. C.; Gavrilova, T. A.; Prosvirin, I. P.; Yang, Y.; Lin; Knappd, M.; Ehrenberg, H. The Crystal Growth and Properties of Novel Magnetic Double Molybdate $RbFe_5(MoO_4)_7$ with Mixed Fe^{3+}/Fe^{2+} States and 1D Negative Thermal Expansion. *Cryst. Eng. Commun.* **2021**, *23*, 3297.
(53) Anantharamaiah, P. N.; Joy, P. A. Enhancing the Strain Sensitivity of $CoFe_2O_4$ at Low Magnetic Fields without Affecting the Magnetostriction Coefficient by Substitution of Small Amounts of Mg for Fe. *Phys. Chem. Chem. Phys.* **2016**, *18*, 10516−10527.
(54) Atuchin, V. V.; Aleksandrovsky, A. S.; Chimitova, O. D.; Diao, C. P.; Gavrilova, T. A.; Kesler, V. G.; Molokeev, M. S.; Krylov, A. S.; Bazarov, B. G.; Bazarova, J. G.; Lin, Z. Electronic Structure of β-RbSm(MoO4)2 and Chemical Bonding in Molybdates. *Dalton Trans.* **2015**, *44*, 1805−1815.
(55) Atuchin, V. V.; Kalabin, I. E.; Kesler, V. G.; Pervukhina, N. V. Nb 3d and O1s Core Levels and Chemical Bonding in Niobates. *J. Electron Spectrosc. Relat. Phenom.* **2005**, *142*, 129−134.
(56) Atuchin, V. V.; Kelser, V. G.; Pervukhina, N. V.; Zhang, Z. Ti 2P and O 1s Core Levels and Chemical Bonding in Titanium-Bearing Oxides. *J. Electron Spectrosc. Relat. Phenom.* **2006**, *152*, 18−24.

https://doi.org/10.1021/acsami.2c23025
ACS Appl. Mater. Interfaces 2023, 15, 15691−15706

(57) Adhikari, R.; Sarkar, A.; Limaye, M. V.; Kulkarni, S. K.; Das, A. K. Variation and Sign Change of Magnetostrictive Strain as a Function of Ni Concentration in Ni-Substituted $ZnFe_2O_4$ Sintered Nanoparticles. *J. Appl. Phys.* **2012**, *111*, No. 073903.
(58) Sowjanya, P.; Kumar, N. P.; Chelvane, A.; Reddy, M. V. R. Synthesis and Analysis of Low Field High Magnetostrictive Ni-Co Ferrite for Magneto-Electric Energy Harvesting Applications. *Mater. Sci. Eng. B* **2022**, *279*, No. 115674.
(59) Anantharamaiah, P. N.; Joy, P. A. Magnetic and Magnetostrictive Properties of Aluminium Substituted Cobalt Ferrite Synthesized by Citrate-gel Method. *J. Mater. Sci.* **2015**, *50*, 6510−6517.
(60) Bhame, S. D.; Bhapkar, A.; Shirolkar, M. M.; Joy, P. A. Magnetostriction Studies on Transition Metal Substituted Cobalt Ferrite. *J. Ind. Chem. Soc.* **2022**, *99*, No. 100599.
(61) Massoudi, J.; Smari, M.; Nouri, K.; Dhahri, E.; Khirouni, K.; Bertaina, S.; Bessais, L.; Hlil, E. K. Magnetic and Spectroscopic Properties of Ni-Zn-Al Ferrite Spinel: From the nanoscale to Microscale. *RSC Adv.* **2020**, *10*, 34556−34580.

https://doi.org/10.1021/acsami.2c23025
ACS Appl. Mater. Interfaces 2023, 15, 15691−15706